

Physics informed neural networks for solving flow problems modeled by the Shallow Water Equations

Xin Qi¹, Gustavo Adolfo Mazza de Almeida¹, and Sergio Maldonado¹

¹University of Southampton

June 23, 2023

Abstract

This paper investigates the application of physics-informed neural networks (PINNs) to solve free-surface flow problems governed by the two-dimensional shallow water equations (SWEs). Two types of PINNs are developed and analysed: a physics-informed fully connected neural network (PIFCN) and a physics-informed convolutional neural network (PICN). The PINNs eliminate the need for labelled data for training by employing the SWEs, initial and boundary conditions as components of the loss function to be minimized. Solutions obtained by both PINNs are compared against those delivered by a finite volume (FV) solver for two idealized problems admitting analytical solutions, and one real-world flood event. The results of these tests show that the prediction accuracy and computation time (i.e., training time) of both PINNs may be less affected by the resolution of the domain discretization than the FV model. Overall, the PICN shows a better trade-off between computational speed and accuracy than the PIFCN. Also, our results for the two idealized problems indicated that PICN and PIFCN can provide more accurate predictions than the FV model, while the FV simulation with coarse resolution (e.g., 5 m and 10 m) outperformed PICN and PIFCN in terms of the speed-accuracy trade-off. Results from the real-world test showed the finely resolved (10 m resolution) FV simulation generally provided the most accurate approximations at flooding peaks. However, both PINNs showed better speed-accuracy trade-off than the FV model in terms of predicting the temporal distribution of water depth, while FV models outperformed the PINNs in their predictions of discharge.

Abstract

This paper investigates the application of physics-informed neural networks (PINNs) to solve free-surface flow problems governed by the two-dimensional shallow water equations (SWEs). Two types of PINNs are developed and analysed: a physics-informed fully connected neural network (PIFCN) and a physics-informed convolutional neural network (PICN). The PINNs eliminate the need for labelled data for training by employing the SWEs, initial and boundary conditions as components of the loss function to be minimized. Solutions obtained by both PINNs are compared against those delivered by a finite volume (FV) solver for two idealized problems admitting analytical solutions, and one real-world flood event. The results of these tests show that the prediction accuracy and computation time (i.e., training time) of both PINNs may be less affected by the resolution of the domain discretization than the FV model. Overall, the PICN shows a better trade-off between computational speed and accuracy than the PIFCN. Also, our results for the two idealized problems indicated that PICN and PIFCN can provide more accurate predictions than the FV model, while the FV simulation with coarse resolution (e.g., 5 m and 10 m) outperformed PICN and PIFCN in terms of the speed-accuracy trade-off. Results from the real-world test showed the finely resolved (10 m resolution) FV simulation generally provided the most accurate approximations at flooding peaks. However, both PINNs showed better speed-accuracy trade-off than the FV model in terms of predicting the temporal distribution of water depth, while FV models outperformed the PINNs in their predictions of discharge.

1 Introduction

Free-surface flow phenomena are usually modeled by the shallow water equations (SWEs), a nonlinear system of partial differential equations (PDEs) governing the evolution of water depth and vertically averaged velocity in the two horizontal dimensions. Over the last decades, significant efforts have been made to approximate the solution to the SWEs in a discretized form through numerical methods, such as Finite Difference (FD) (e.g., Casulli, 1990; Molls & Chaudhry, 1995; Kurganov & Levy, 2002, and others), Finite Volume (FV) (e.g., Alcrudo & Garcia-Navarro, 1993; Bale et al., 2003; Botta et al., 2004; Yoon & Kang, 2004; Toro & Garcia-Navarro, 2007, and others), or Finite Element (FE) (e.g., Lynch & Gray, 1979; Hanert et al., 2005; Dawson et al., 2006; Marras et al., 2016, and others). These methods are now well-established and have been the object of extensive tests and validation (e.g., Toro & Garcia-Navarro, 2007; Wilson et al., 2007; Liang & Marche, 2009; LeVeque et al., 2011, and others). While the ability of these models to capture the main properties of free-surface flows has been widely verified, accurate solutions to real-world problems typically require the use of a finely resolved computational mesh, which tends to significantly increase the computational cost (Bernard et al., 2009; Liang, 2011; Juez et al., 2014). In explicit schemes for the solution of the 2D SWEs, the computational cost C scales cubically with the size of the computational grid Δx (i.e., $C \sim \Delta x^{-3}$). As a result, important applications such as large-scale flood simulations are often beyond the capabilities of available numerical methods given existing computational resources. This is particularly challenging when simulations need to be performed in real-time, or as part of a probabilistic flood risk analysis (Leskens et al., 2014; Sanders & Schubert, 2019; Ferrari & Vacondio, 2022; J. Li et al., 2022). For example, flood risk management usually requires the simulation of a large number of inundation scenarios, which may increase the overall computational time by orders of magnitude. Although the computational speed of models can be improved by using state-of-the-art hardware and parallel computing algorithms (Leandro et al., 2014; Monnier et al., 2016), such techniques may still be insufficient to meet the computational requirements of many important applications (Kabir et al., 2020). Owing to these limitations, a cost-effective model for free-surface problems may offer an appealing alternative.

63 Over the last decades, Machine Learning (ML) models, and Artificial Neural Net-
64 works (ANNs) in particular, have found a wide range of applications, such as in finan-
65 cial prediction (Henrique et al., 2019), facial recognition (Sulavko, 2020), supply chain
66 optimization (Carbonneau et al., 2008), radiation forecasting (El Naqa et al., 2015), and
67 automatic cancer screening (William et al., 2018), to cite only a few. The extraordinary
68 increase in applications of ML models is largely due to their ability to mathematically
69 describe any nonlinear relationship between inputs and outputs according to the univer-
70 sal approximation theorem (Hornik et al., 1989), the increasing availability of data for
71 training, and increasing computational power.

72 The first works using ML for the solution of problems governed by the SWEs are
73 relatively recent and focused on the development of simple meta-models (e.g., Kabir et
74 al., 2020; Liu & Pender, 2015; Bermúdez et al., 2019; Mahesh et al., 2022, and others).
75 In this type of model, ML is used to build a prediction model to describe the input-output
76 relationship previously obtained through the solution of the governing PDEs by another
77 numerical approximation model; i.e. the ML model thus becomes a surrogate model. These
78 surrogate models typically need to be trained using the results of a large number of nu-
79 merical simulations conducted at fine resolution, which can be very computationally de-
80 manding.

81 Physics-Informed Neural Networks (PINNs), for which data (and therefore expen-
82 sive numerical simulations) are not required for training, have gained increasing atten-
83 tion in recent years (Pang et al., 2019; Mao et al., 2020; Cai et al., 2021; Krishnapriyan
84 et al., 2021; Jin et al., 2021). A PINN is essentially a ML algorithm which uses the in-
85 formation contained in the physical laws (such as the governing PDEs, boundary and
86 initial conditions) to train the model. This eliminates the need for training data and thus,
87 expensive numerical simulations. A data-free PINN is required to satisfy the governing
88 PDEs, Initial Conditions (ICs) and Boundary Conditions (BCs) simultaneously. Recent
89 applications of ML algorithms to solve complex physics phenomena have focused on the
90 use of Deep Learning (DL) models (e.g., Sun et al., 2020; Zhang et al., 2020; Haghighat
91 et al., 2020; Vlassis & Sun, 2021, and others). DL is a form of ANN with more than one
92 hidden layer, which provides the complexity required to model intricate nonlinear rela-
93 tionships, such as those found in computer vision (Voulodimos et al., 2018), health man-
94 agement (Khan & Yairi, 2018), language translation (Rastgoo et al., 2021), and remote
95 sensing (X. X. Zhu et al., 2017). In the past few years, a large number of data-free PINNs
96 have been developed by employing DL techniques, such as the Fully Connected Neural
97 Networks (FCNNs) and Convolutional Neural Networks (CNNs). For example, in Raissi
98 et al. (2019) several FCNNs were trained to predict the solutions to various systems of
99 PDEs, including Allen–Cahn, Schrödinger, Navier–Stokes, and Korteweg–de Vries equa-
100 tions. In the context of fluid dynamics, other implementations of FCNNs include those
101 of Sun et al. (2020) and Mao et al. (2020), who used their DL models to find solutions
102 to the Navier–Stokes (in steady state) and Euler equations (involving shock waves), re-
103 spectively. The use of CNNs has also been explored, for instance, for problems governed
104 by the Navier–Stokes (Cai et al., 2021) and Boltzmann transport equations (R. Li et al.,
105 2021), or for predicting steady flow in random heterogeneous media (Y. Zhu et al., 2019).
106 The success of these works shows that data-free PINNs should be considered as serious
107 contenders for solving flow problems that are typically modelled by PDEs, and which
108 have been traditionally solved using conventional numerical methods (FD, FV, etc.).

109 While ML trained from labeled data (i.e., mainly conventional numerical solutions)
110 has been used to solve the SWEs (e.g., Mahesh et al., 2022; Ștefănescu et al., 2014; Yıldız
111 et al., 2021; C. Li et al., 2023, and others), to the authors’ knowledge only a very lim-
112 ited number of articles (e.g., Bihlo & Popovych, 2022) has been published so far on the
113 use of a data-free PINNs for this purpose. In Bihlo and Popovych (2022), a PINN (specif-
114 ically, based on a FCNN) was employed to find solutions to the SWEs on a spherical do-
115 main, and the focus was on idealized problems which may find applications in meteo-

116 rology. Whether a similar DL technique may be used to accurately and efficiently solve
 117 challenging free-surface flow problems involving friction and complex boundary condi-
 118 tions, such as large-scale simulations of flow over complex topography in rivers and coastal
 119 areas, remains an open question.

120 The solution of PDEs, and in particular of the SWEs, using PINN algorithms is
 121 still in its infancy and further investigation is required to understand the main charac-
 122 teristics of solutions obtained by these methods. Firstly, the trainset for PINNs needs
 123 to be generated from a particular, discrete, set of points. It remains unclear how accu-
 124 racy and computational performance (i.e., training speed) depend on the discretization
 125 of the domain. Additionally, both FCNNs and CNNs are commonly used DL models in
 126 the research field of PINN. However, in a specific problem governed by a system of PDEs,
 127 it is usually difficult to determine which one will deliver the best performance before car-
 128 rying out tests.

129 The aim of this paper is to develop and test two different PINN models to approx-
 130 imate solutions to various free-surface flow problems governed by the 2D SWEs. The PINN
 131 models are based on the FCNN and CNN approaches, and are hereafter referred to as
 132 PIFCN (physics informed fully connected network) and PICN (physics informed convo-
 133 lutional network), respectively. These models are data-free in that they do not require
 134 data from separate numerical simulations, or laboratory/field measurements, to train the
 135 networks. In this paper both PIFCNs and PICNs are compared against the Finite Vol-
 136 ume (FV) solver of the 2D SWE developed by de Almeida et al. (2016) through a set
 137 of test cases including two idealized flow problems and one real-world flood event. The
 138 rest of this paper is organized as follows. First, the governing equations and the frame-
 139 work of both PINNs are described in Section 2. This section also provides a concise re-
 140 view of FCNNs and CNNs. In Section 3, the accuracy and computational performance
 141 of the proposed physics-informed networks (PIFCN and PICN) are investigated for the
 142 three test cases. The main outcomes of the study are discussed and summarized in Sec-
 143 tion 4.

144 2 Methods

145 2.1 Overview

146 Most problems requiring the simulation of free-surface flows in the horizontal plane,
 147 such as flow in rivers and estuaries, dam-breaks, and flood wave propagation can be mod-
 148 eled by the SWEs. The 2D SWEs represent a system of nonlinear, hyperbolic PDEs de-
 149 scribing the conservation of water mass and depth-average momentum, which can be ex-
 150 pressed as:

$$\frac{\partial \mathbf{U}}{\partial t} + \frac{\partial \mathbf{F}(\mathbf{U})}{\partial x} + \frac{\partial \mathbf{G}(\mathbf{U})}{\partial y} = \mathbf{S}(\mathbf{U}); \quad (1)$$

$$\mathbf{U} = \begin{bmatrix} h \\ hu \\ hv \end{bmatrix}, \quad \mathbf{F}(\mathbf{U}) = \begin{bmatrix} hu \\ hu^2 + \frac{1}{2}gh^2 \\ huv \end{bmatrix}, \quad \mathbf{G}(\mathbf{U}) = \begin{bmatrix} hv \\ huv \\ hv^2 + \frac{1}{2}gh^2 \end{bmatrix}, \quad \mathbf{S}(\mathbf{U}) = \begin{bmatrix} 0 \\ gh(s_{ox} - s_{fx}) \\ gh(s_{oy} - s_{fy}) \end{bmatrix}, \quad (2)$$

151 where x and y are the spatial (horizontal) coordinates; t is time; $h(x, y, t)$ is the water
 152 depth; $u(x, y, t)$ and $v(x, y, t)$ denote the x and y components of the depth-averaged flow
 153 velocity, respectively; $s_{ox} = -\partial z/\partial x$ and $s_{oy} = -\partial z/\partial y$ are the bed slopes in the x
 154 and y directions, respectively, and $z(x, y)$ is the terrain elevation (assumed constant in
 155 time); s_{fx} and s_{fy} denote the friction slopes in the x and y directions, respectively. The
 156 friction slopes can be modeled using Manning-Strickler's expression, $s_{fx} = n^2 u \sqrt{u^2 + v^2} h^{-4/3}$,
 157 $s_{fy} = n^2 v \sqrt{u^2 + v^2} h^{-4/3}$, where n is the Manning coefficient. Solutions $\mathbf{U} = (h, hu, hv)^T$
 158 to this system (subject to well-posed boundary and initial conditions) can be computed
 159 by several numerical methods available, as discussed in the Introduction.

In this paper we propose a ML-based solution to this problem, whereby the input layer \mathbf{x} represents the independent variables and parameters of the problem, $\mathbf{x} = (x, y, t, n, z)$, and the trained model \aleph is expected to provide an approximate solution for $h(\mathbf{x})$, $hu(\mathbf{x})$ and $hv(\mathbf{x})$ in the corresponding domain; in other words:

$$\mathbf{U}(\mathbf{x}) \cong \tilde{\mathbf{U}}(\mathbf{x}) = \aleph(\mathbf{x}; \Gamma), \quad (3)$$

160 where $\tilde{\mathbf{U}}(\mathbf{x})$ denotes the output from the PINN, which is in turn defined by the group
 161 of trainable parameters Γ (e.g., convolutional filter, weights and biases). The PINN mod-
 162 els proposed in this paper are trained by minimizing the composite loss function, defined
 163 as:

$$\mathcal{L} = \lambda_1 \cdot \mathcal{L}_p + \lambda_2 \cdot \mathcal{L}_b + \lambda_3 \cdot \mathcal{L}_0, \quad (4)$$

164 where \mathcal{L} (a scalar) is the loss function to be minimized, λ_{1-3} are the vectors of penalty
 165 coefficients for every specific loss term; namely, \mathcal{L}_p penalizes the residuals of the SWEs,
 166 \mathcal{L}_b and \mathcal{L}_0 penalize the BCs (subscript b) and ICs (subscript 0) residuals, respectively.
 167 These loss terms are in turn given by:

$$\mathcal{L}_p = \frac{1}{N} \sum_{i=1}^N |\partial_t \tilde{\mathbf{U}}_i + \partial_x \mathbf{F}(\tilde{\mathbf{U}}_i) + \partial_y \mathbf{G}(\tilde{\mathbf{U}}_i) - \mathbf{S}(\tilde{\mathbf{U}}_i)| \quad (5a)$$

$$\mathcal{L}_b = \frac{1}{N_b} \sum_{i=1}^{N_b} |\tilde{\mathbf{U}}_{b,i} - \mathbf{U}_{b,i}| \quad (5b)$$

$$\mathcal{L}_0 = \frac{1}{N_0} \sum_{i=1}^{N_0} |\tilde{\mathbf{U}}_{0,i} - \mathbf{U}_{0,i}| \quad (5c)$$

168 The tilde symbol ($\tilde{}$) denotes neuronal network output and the subscript $i \in [1, N]$
 169 refers to the i^{th} collocation point. N represents the number of collocation points, which
 170 in this paper is defined from a uniformly discretized domain of the independent variables
 171 $N = n_x \times n_y \times n_t$, where n_x , n_y and n_t are the number of points used to discretize the
 172 domain along the x , y and t coordinates, respectively. The boundaries of the spatio-temporal
 173 domain are represented by a subset of N ; in particular, the model will employ $N_b < N$
 174 and $N_0 < N$ points to define the BCs and ICs, respectively.

175 For each approximate solution produced by the PINN, the partial derivatives in
 176 Eq. 5a are computed through the method of automatic differentiation (autodiff) (Paszke
 177 et al., 2017), which back-propagates derivatives from the outputs to the targeted inputs
 178 through the chain rule to compute the desired derivatives (Cai et al., 2021; Baydin et
 179 al., 2018). Thus, the partial derivatives of the approximate solution with respect to the
 180 independent variables can be computed without the errors common to numerical differ-
 181 entiation techniques. The loss function is minimised using the gradient descent method,
 182 with gradients of the loss function with respect to trainable parameters computed by back-
 183 propagation. These parameters can be updated either using all, or a subset (batch) of
 184 the collocation points.

185 One significant difficulty of solutions to flow problems modeled by the SWEs is the
 186 so-called wet-dry front issue (i.e., moving boundary). Physically, the value of the flow
 187 depth h cannot be negative. Areas of the domain where such solutions may be obtained
 188 correspond to dry areas, which are not governed by the SWEs. To overcome this prob-
 189 lem, we set $\mathcal{L}_p = 0$ if the predicted value of \tilde{h} is negative. This ensures that the model
 190 does not penalize making predictions outside the wet domain.

191 Figure 1 shows a diagram illustrating the overall modeling framework proposed in
 192 this paper for solving the SWEs by a PINN method. Note that the collocation points

193 can be chosen randomly in the space-time domain and their number prescribed. The general
 194 steps are outlined below.

- 195 1. Define the architecture of the PINN
 196 2. Initialize the hyperparameters for the PINN
 197 3. Compute the outputs from the PINN with given inputs
 198 4. Compute the derivatives with respect to x, y, t and the corresponding loss \mathcal{L}
 199 5. Update the PINN based on \mathcal{L}
 200 6. Repeat steps 3 to 5 until the end of the user-prescribed number of training epochs

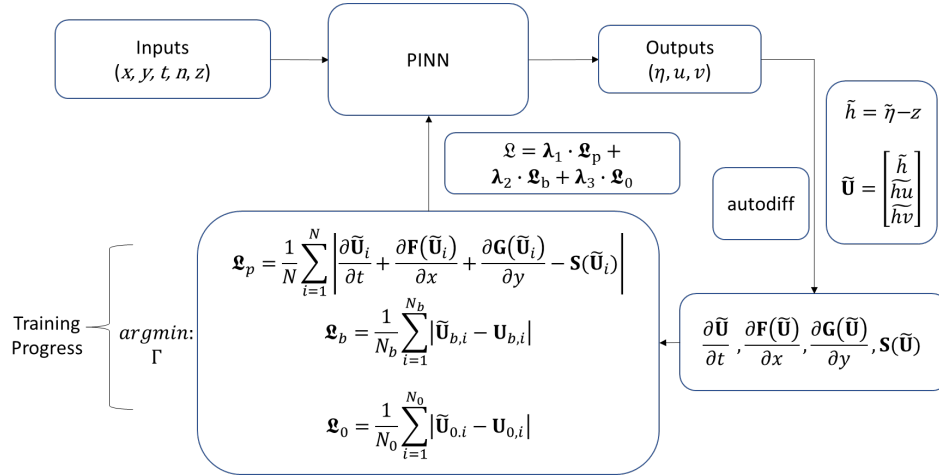


Figure 1. A schematic diagram of a physics informed neuronal network (PINN) for finding approximate solutions to the shallow water equations.

201 2.2 Fully Connected Neural Network

202 The FCNN is the most commonly applied ML model and often includes more than
 203 one hidden layer. Every hidden layer receives the signals from the previous layer, per-
 204 forms basic computations defined at each neuron, and passes the results to the next layer
 205 (Haykin, 2009). Figure 2 shows a diagram of a FCNN. Mathematically, the basic function
 206 of the output for the j^{th} hidden layer \mathbf{y}_j is:

$$\mathbf{y}_j = \varphi(\mathbf{W}_j \mathbf{y}_{j-1} + \mathbf{b}_j) \quad (6)$$

207 where \mathbf{W} is the matrix of weights, \mathbf{b} is the vector of biases and $\varphi(\cdot)$ is the activation func-
 208 tion.

209 In the proposed method, solutions for each output variable $\eta(\mathbf{x}) = h(\mathbf{x}) + z$, $hu(\mathbf{x})$,
 210 $hv(\mathbf{x})$ are approximated by 3 separate FCNNs with the same structure, as illustrated in
 211 Figure 2. Every FCNN receives the same raw inputs. As a result, the trainable param-
 212 eters of the solution for each output variable are decoupled. This can significantly im-
 213 prove the prediction accuracy in multivariate problems, especially when the distributions
 214 and magnitudes of the variables are significantly different (e.g., Sun et al., 2020; Gao et
 215 al., 2021; Guo et al., 2020, and others).

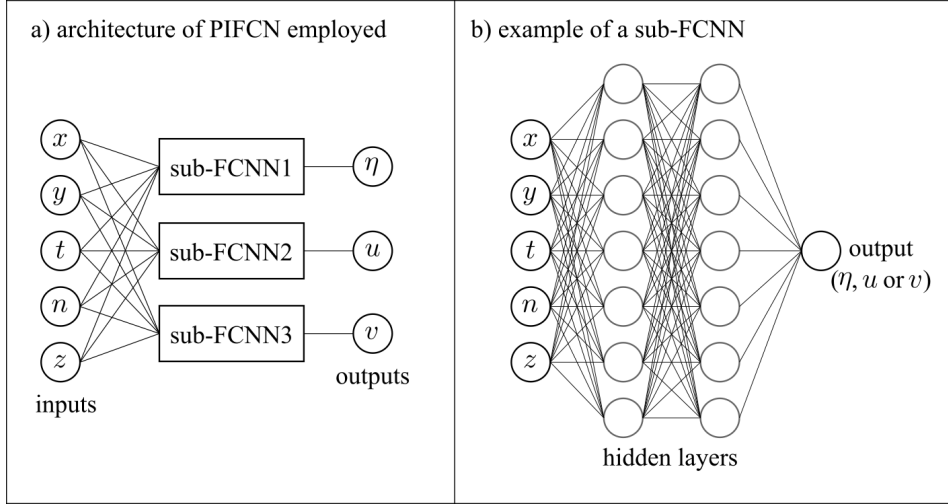


Figure 2. (a) The architecture of the physics-informed fully connected networks (PIFCNs) employed in this paper. (b) An example of a typical fully connected neuronal network (FCNN) which is employed as a sub-network within the PIFCN to predict each individual output; as illustration, 2 hidden layers with 7 neurons each are shown, but these hyperparameters are varied in this study.

216

2.3 Convolutional Neural Network

217

218

219

The CNN adds one or more convolutional layers that extract features of the raw training dataset before feeding this onto the typical hidden layers used to build FCNNs. The general expression for the convolution operator \star with 1 stride is:

$$(\mathbf{s} \star \mathbf{k})_i = \sum_{j=1}^n k_j s_{i+j-1} \quad i = 1, 2, \dots, m - n + 1 \quad (7)$$

220

221

222

223

224

225

where \mathbf{s} denotes the input signal vector of length m (in this paper, this is \mathbf{x}), and \mathbf{k} denotes the trainable filter of length n . The convolution operation is to slide the preset convolutional filter over the signal input and output the signal with a shorter length (i.e., the input vector is shortened by $n - 1$ elements). The shorter length of the convolved output signal allows the following typical hidden layer to have fewer neurons, facilitating the network's learning of large-scale problems with high complexity (Gao et al., 2021).

226

227

228

229

Figure 3 shows the structure of the CNN used in this paper. The trainset is generated from a number of points (i.e., collocation points) randomly sampled from a grid of equally spaced points. Each output variable, $h(\mathbf{x})$, $hu(\mathbf{x})$, $hv(\mathbf{x})$, is also predicted by a separate sub-CNN.

230

2.4 PINN design

231

232

233

234

235

236

237

The accuracy and computational performance of the PINNs described in the previous sections will be assessed and compared against the corresponding performance and solutions by a conventional FV model. There is currently no universal design approach to determine the optimal, or even appropriate, structure for a neural network (Bihlo & Popovych, 2022). The general selection rule for PINN design is to find a structure with the lowest possible complexity that achieves the desired accuracy of prediction. This rule can usually help provide an AI model with quick learning speed and improved predic-

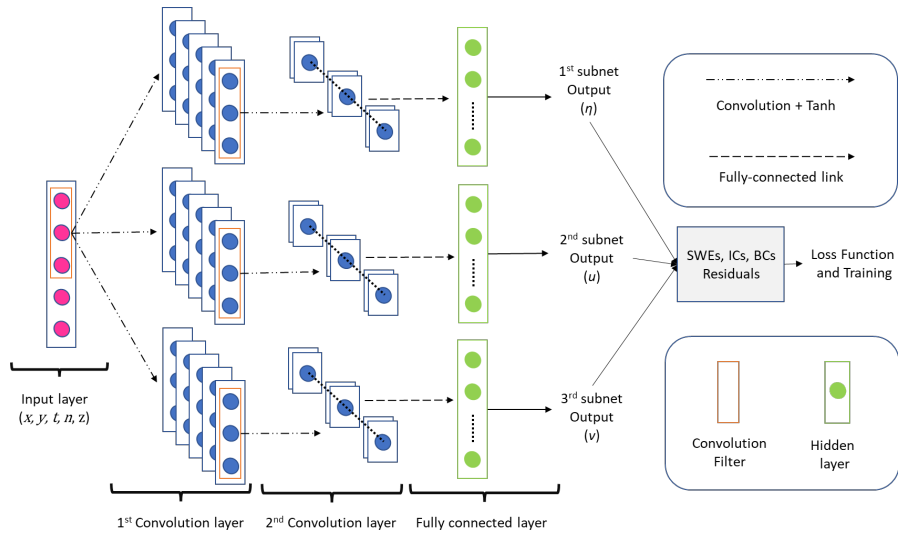


Figure 3. An example of the structure of a CNN-based model with 3 subnets for solving free-surface flow problems. Each output variable (η , u or v) is approximated by a separate CNN with the above structure; all sub-networks receive the same inputs. Each CNN has two convolutional layers and one hidden layer. The hyperparameters shown in the figure are discussed in Section 2.4.

238 tion capabilities while avoiding overfitting issues (Blumer et al., 1987). In this paper, the
 239 final decision for the model structure (i.e. hyperparameters such as the number of neurons,
 240 hidden layers, and convolutional layers and channels in the case of CNN) was made
 241 after many practical attempts (see Appendix A). As the evaluation of the PINNs per-
 242 formance in this paper consists of two, often competing, criteria (accuracy and compu-
 243 tational cost), it may be difficult to find a single assessment metric to guide the PINNs
 244 design. Hence, we give priority to accuracy by gradually increasing the complexity of the
 245 PINNs until similar or higher accuracy than benchmark results (e.g. from an analyti-
 246 cal solution or a finely resolved FV simulation) is attained. Generally, in our design it-
 247 erations, the number of hidden layers and the corresponding neurons for building PINNs
 248 (i.e., PIFCN and PICN) started from 1 and 50, respectively. The number of convolutional
 249 layers and corresponding channels started from 1 and 5, respectively. For both PICN and
 250 PIFCN we use the hyperbolic tangent activation function (Tanh). Note that the PINN
 251 design may change significantly depending on domain and flow conditions; i.e., it can be
 252 very problem-specific. It is also important to recognize that the networks chosen do not
 253 represent the strictly optimal structure, but only the best out of the subset of structures
 254 that were tested.

255 For improving the learning speed and reducing the effect of parameter initializa-
 256 tion, the Batch Normalization method of Ioffe and Szegedy (2015) was used, which nor-
 257 malizes the signals between adjacent convolutional or hidden layers. The Adam optimizer
 258 (Kingma & Ba, 2014), along with the ‘1-cycle’ (Smith & Topin, 2019) strategy was used
 259 to control the training of the PINNs. The PINNs were implemented on the Pytorch plat-
 260 form Paszke et al. (2017). The FV simulation and the training of the PIFCNs and PICNs
 261 were performed using the University of Southampton’s supercomputer Iridis 5 ensuring
 262 that the exact same hardware resources were employed (thus ensuring a fair compari-
 263 son across all simulations performed).

264 3 Case studies

265 This section describes three case studies used to test the PINNs, comparing their
 266 results against analytical and numerical (Finite Volume) solutions. The first and second
 267 tests are idealized 1D (unsteady and steady, respectively) flow problems for which an-
 268 analytical solutions are available. However, simulations were performed on a 2D domain
 269 since the ultimate aim is to employ the PINNs developed here in 2D flow problems. The
 270 third test case is an unsteady two-dimensional simulation of a real-world flood event that
 271 took place in the Tiber river, Italy. This case study has been previously employed to eval-
 272 uate the performance of other numerical models (e.g., Morales-Hernández et al., 2016;
 273 Shamkhalchian & de Almeida, 2021, and others).

274 Topographic data used in all tests are defined by square grids with different res-
 275 olutions. The grid points are used to generate a triangular mesh for the FV model. These
 276 are also employed, along with defined temporal steps, as the collocation points for the
 277 PINNs training. The accuracy of the solutions will be assessed by the root mean square
 278 error, \mathcal{R} , of the outputs of each model relative to the benchmark solution. For example,
 279 in the evaluation of accuracy for the prediction of h with N_p output points, the perfor-
 280 mance metric is defined as $\mathcal{R}_h = \sqrt{\sum (h_i - \tilde{h}_i)^2 / N_p}$, where h_i is the benchmark solu-
 281 tion (i.e., the analytical solution when available, or the solution of the FV model at fine
 282 resolution). The second performance metric we employ is the computational cost, \mathcal{T}_c , which
 283 represents training time for the PINNs (PICN and PIFCN), and run time for the FV model.
 284 In the results presented in the following sections, predictions by the FV, PIFCN and PICN
 285 models are labelled with the different resolutions used. For example, FV (10) represents
 286 a 10 m resolved simulation using the FV hydraulic model, and PICN (50) refers to the
 287 prediction of the PICN trained from a 50 m resolved dataset.

288 3.1 Flood wave propagation over a horizontal plane

289 The first test case is a one-dimensional simulation of an inundation wave propa-
 290 gating over a horizontal bed. A time-dependent BC is imposed at $x = 0$. Under the
 291 idealized assumption of a flow velocity that is constant in space and time, the problem
 292 admits an analytical solution which can be expressed as (Hunter et al., 2005):

$$293 \quad h_a(x, t) = \left\{ \frac{7}{3} (n^2 u^2 (x - ut)) \right\}^{3/7}, \quad (8)$$

294 where the subscript a is used to denote the analytical solution. The domain used is a
 295 100 m wide, 1200 m long channel. The constant velocity is set as $u(x, t) = 0.29 \text{ ms}^{-1}$
 296 and the boundary condition $h(x = 0, t)$ is given by Eq. 8. The domain is initially dry,
 297 i.e., $h(x, t = 0) = 0$. Manning's coefficient n is set to $0.03 \text{ sm}^{-1/3}$. The duration of
 298 the simulation is 3600 s. The FV model was run at resolutions of 1, 2, 5 and 10 m, while
 299 the PINN models were trained with datasets defined at resolutions of 10, 25, 50 and 100
 300 m. While the time step of the explicit FV scheme is controlled by the Courant-Friedrichs-
 301 Lewy (CFL) stability condition, the regression approximation implemented by the PINN
 302 model is not limited by temporal resolution. However, the time step adopted to train
 303 the PINN model is a factor that clearly affects both accuracy and computational per-
 304 formance. For this test, we use a temporal resolution for the PINN of 300 s. The selected
 batch size is set as the full set of collocation points $n_x \times n_y \times n_t$.

305 The architecture of the PICN consists of 2 convolutional layers (the first and sec-
 306 ond layers have 5 and 20 channels, respectively) and 1 fully connected hidden layer with
 307 50 neurons. The architecture for the PIFCN consists of 3 fully connected hidden layers,
 308 each of which has 1000 neurons.

309 Figures 4 and 5 illustrate the values of $h(x, y = 50\text{m})$ and $hu(x, y = 50\text{m})$ (left
 310 vertical axes), and the corresponding error (right vertical axes) $\epsilon_h(x, y = 50\text{m}) = h(x, y =$

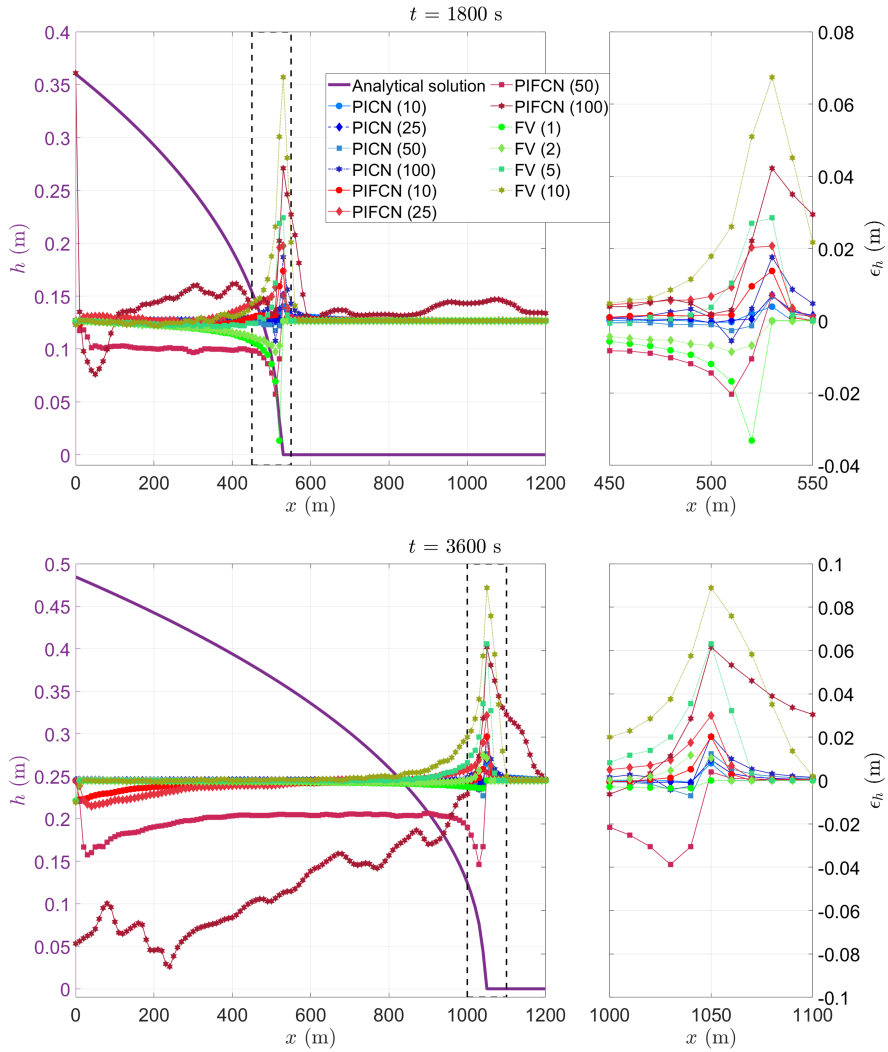


Figure 4. Test 1: Longitudinal profiles ($y = 50 \text{ m}$) of water depth errors ϵ_h relative to the analytical solution obtained by each of the models at $t = 1800 \text{ s}$ (top) and $t = 3600 \text{ s}$ (bottom), shown against right y -axis. The analytical solution for h (purple line) is plotted against the left y -axis; note that the right-side figure is the enlarged version of the rectangular box in the left-side figure; both figures share the same right y -axis.

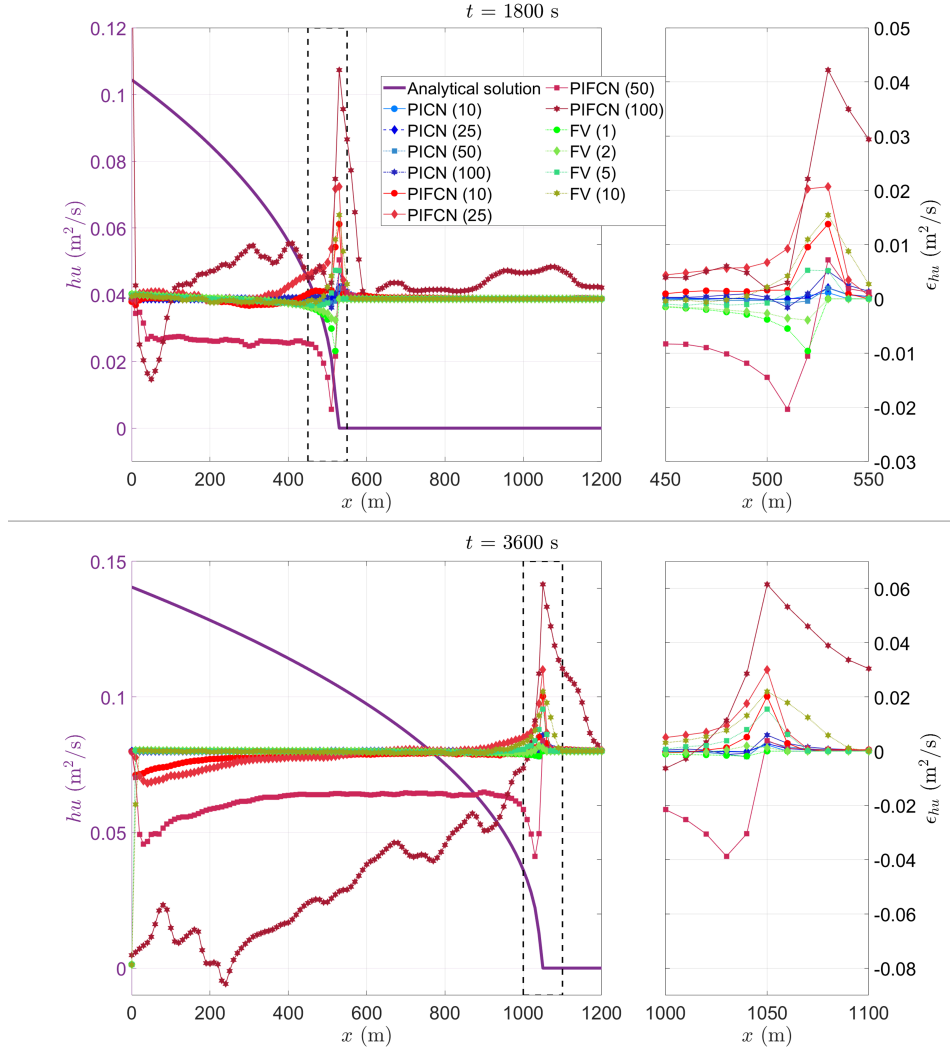


Figure 5. Test 1: Longitudinal profiles ($y = 50$ m) of water depth errors ϵ_{hu} relative to the analytical solution obtained by each of the models at $t = 1800$ s (top) and $t = 3600$ s (bottom). The analytical solution for hu (purple line) is plotted against the left y -axis; note that the right-side figure is the enlarged version of the rectangular box in the left-side figure; both figures share the same right y -axis.

311 $50\text{m}) - h_a(x, y = 50\text{m})$ and $\epsilon_{hu}(x, y = 50\text{m}) = \tilde{h}u(x, y = 50\text{m}) - (hu)_a(x, y = 50\text{m})$
 312 computed by all three models at $t = 1800$ and 3600 s, respectively. Values of hv are not
 313 reported as the test case is fundamentally one-dimensional. Overall, all the water depth
 314 predictions, with the exception of PIFCN (100), show good agreement with the analyt-
 315 ical solution (i.e. most results displaying $|\epsilon| < 0.01\text{m}$). As the position of the wet-dry
 316 front predicted by the models does not exactly match the analytical solution, and the
 317 front is steep at that point, errors are larger in this region. PICN and FV both show sim-
 318 ilar prediction accuracy of both h and hu , whereas PIFCNs with coarsely resolved train-
 319 sets (i.e., 50 m and 100 m) provide higher prediction errors of hu .

320 Figure 6 shows \mathcal{R}_h (relative to the analytical solution h_a) for all results obtained
 321 with the PICN, PIFCN, and FV models as a function of the corresponding computational
 322 time \mathcal{T}_c . The sum to compute \mathcal{R}_h is over all collocation points; i.e., spanning the whole
 323 spatio-temporal domain. In this figure, the various points (blue and red) presented for
 324 each PINN model represent solutions obtained at different epochs during the training
 325 of the networks, which correspond to different computation time and level of accuracy.
 326 The green cross points represent the simulation accuracy and computation time for the
 327 FV model. The results in this figure are based on model (i.e. PICN, PIFCN, and FV)
 328 outputs at the same grid points selected from the entire domain with a spatial and tem-
 329 poral resolution of 10 m and 360 s. Predictions of hu follow the general pattern observed
 330 for h on Figure 6 and are not reported here to avoid repetition. Figure 6 allows us to
 331 comparatively assess the performance of the models tested in terms of their speed-accuracy
 332 trade-off. Based on this criterion, a model performs better than another when it provides
 333 more accurate results under the same computational time, or vice-versa; in other words,
 334 the best results are those closest to the bottom left corner of the plot.

335 Figure 6 shows that FV (10) and FV (5) produce sub-centimetre \mathcal{R}_h (which is usu-
 336 ally considered a good level of accuracy for many applications) at least one order of mag-
 337 nitude faster than the PINN models, whereas FV (2) takes slightly longer than PICNs
 338 (for the same level of accuracy), and FV (1) only outperforms PIFCN (10) in terms of
 339 the speed-accuracy trade-off. All PINNs except PIFCN (100) show the potential to achieve
 340 better accuracy of prediction than the FV model at the highest resolution tested here
 341 (1 m), provided they are trained for long enough. PICNs provide a faster solution (for
 342 similar \mathcal{R}_h values) than PIFCNs. Also, for PIFCN, the trainset size (which in this case
 343 is determined by the resolution) did not significantly affect its maximum accuracy at res-
 344 olutions ≤ 50 m, whereas the accuracy of the FV model continues to improve as the mesh
 345 is refined below 10 m.

346 3.2 Subcritical steady flow over an undulating bed

347 The second test case represents a 1D, steady, non-uniform flow over an undulat-
 348 ing bed, for which an analytical solution is available (see MacDonald, 1996; de Almeida
 349 & Bates, 2013; Delestre et al., 2013). This test case will be used to evaluate the solu-
 350 tion obtained by the PICN and PIFCN in a problem with variable topography. The (rect-
 351 angular) channel is 1000 m long, and Manning’s coefficient n is set to $0.03 \text{ sm}^{-1/3}$. The
 352 constant inflow discharge per unit width of the channel is $q_x = uh = 2 \text{ m}^2\text{s}^{-1}$, and the
 353 downstream water depth is $\frac{9}{8}$ m. We prescribe the following function representing the
 354 water depth $h(x)$ (which is the benchmark solution against which the PINN approxima-
 355 tions will be compared):

$$h(x) = \frac{9}{8} + \frac{1}{4} \sin\left(\frac{\pi x}{500}\right). \quad (9)$$

356 We model this 1D problem in a 2D domain using a width of 50 m (and $q_y = 0$)
 357 for the reasons discussed previously. Also, although the solution sought is for a steady
 358 flow problem, the steady condition was reached via an unsteady flow simulation, as the

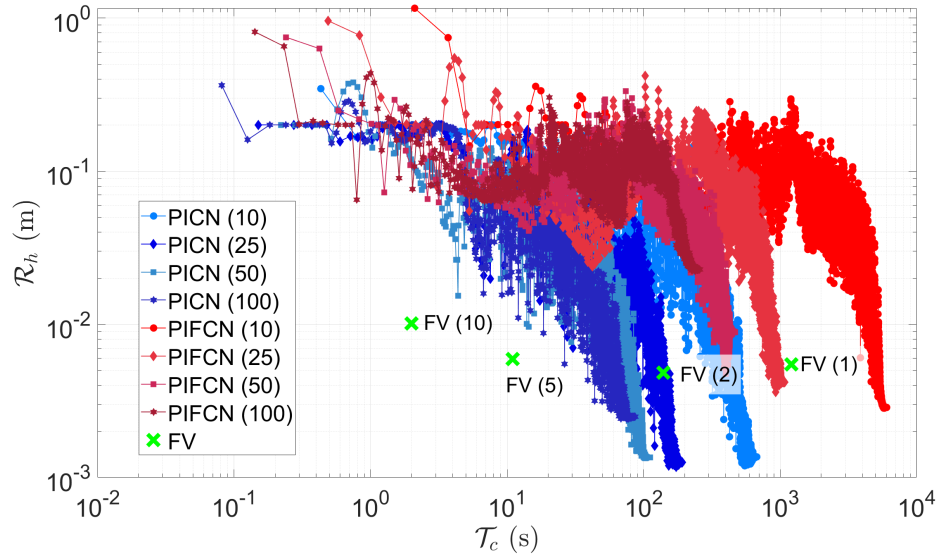


Figure 6. Test 1: Values of \mathcal{R}_h as a function of \mathcal{T}_c (training time for PICN and PIFCN and run time for FV); note that the right-most point of each cloud corresponds to the highest accuracy that any given PINN can achieve. The number in brackets represents the resolution (in meters) of the training data set (for PICN and PIFCN) or mesh (for the FV model).

359 object of this paper is to test approximate methods to solve the time-dependent SWEs.
 360 The unsteady simulations were run from an initially dry domain over a period of 20 hours,
 361 whereby the upstream BCs increase linearly with time from zero to the aforementioned
 362 constant values over the first 10 hours of the simulation.

363 The training dataset for PICN and PIFCN was obtained from grids resolved at 5,
 364 10, 25 and 50 m at the following times: 0, 1, 3, 5, 10, 15 and 20 hours. The selected batch
 365 size is $2/7 \times N$, where the value $2/7$ comes from trial and error (larger batch sizes de-
 366 creased the accuracy of the results). The FV model was run at resolutions of 2, 5 and
 367 10 m.

368 For this case, the architecture of the PICN consists of 2 convolutional layers (the
 369 first and second layers have 5 and 20 channels, respectively) and 1 fully connected hid-
 370 den layer with 50 neurons (same as in Test 1). The architecture of the PIFCN consists
 371 of 3 fully connected hidden layers, each of which has 1000 neurons (different from Test
 372 1).

373 Figure 7 shows the analytical curve for depth profile at the centre of the channel
 374 $h(x, y = 30 \text{ m})$ (left axis) and the corresponding errors of each of the approximate so-
 375 lutions ϵ_h (right axis) predicted by the PICN (blue points), PIFCN (red points), and FV
 376 models (green points). Figure 8 presents similar results but for the variable hu . As the
 377 analytical solution is for the steady state, only the results at the end of the simulations
 378 are assessed. Overall, all models tested delivered results at sub-centimeter level of ac-
 379 curacy for h . The three PICNs showed the lowest errors of both h and hu , followed by
 380 FV (2). Values of ϵ_{hu} obtained from FV models display small (mostly within 1% of the
 381 actual value of hu) spatial variations, while they nearly are constant for both PIFCN and
 382 PICN.

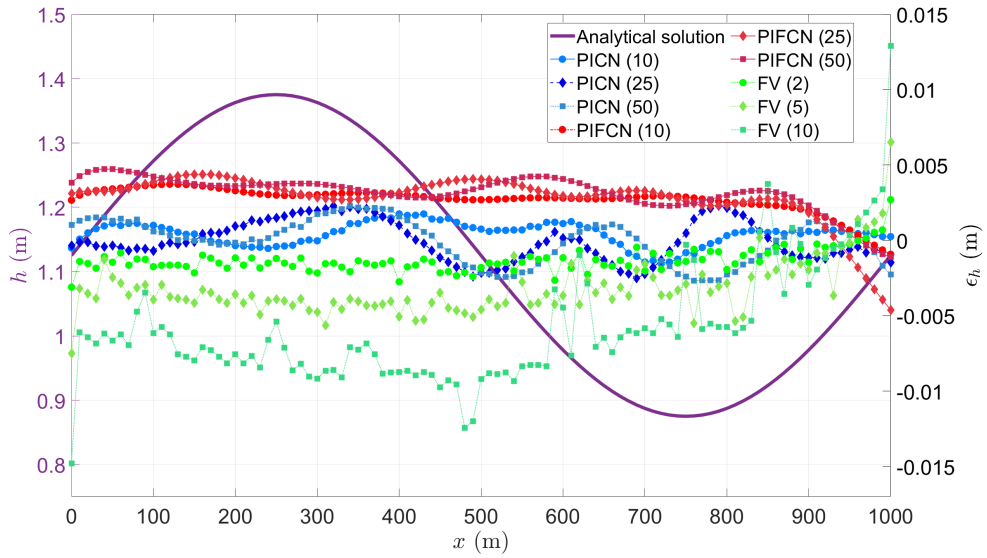


Figure 7. Test 2: Longitudinal profiles ($y = 30$ m) of water depth errors obtained by each of the models at the end of the simulation/training (right y -axis). The analytical solution h (purple line) is plotted against the left y -axis.

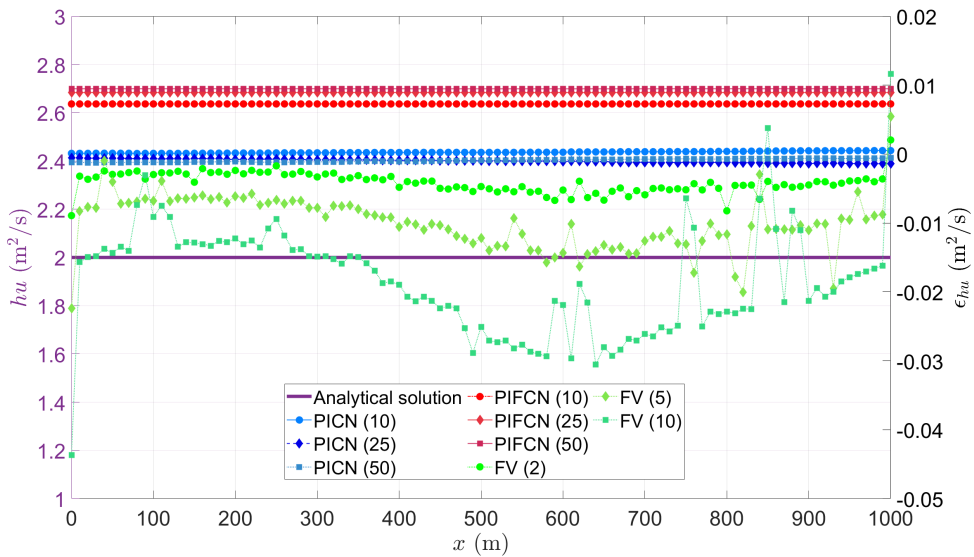


Figure 8. Test 2: Longitudinal profiles ($y = 30$ m) of water depth errors obtained by each of the models at the end of the simulation/training (right y -axis). The analytical solution hu (purple line) is plotted against the left y -axis.

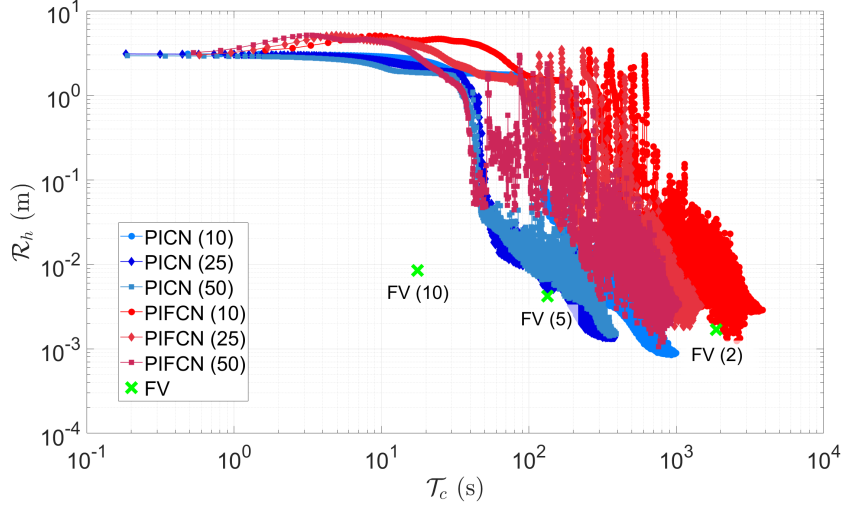


Figure 9. Test 2: Values of \mathcal{R}_h as a function of \mathcal{T}_c (training time for PICN and PIFCN and run time for FV); note that the right-most point of each cloud corresponds to the highest accuracy that any given PINN can achieve. The number in brackets represents the resolution (in meters) of the training data set (for PICN and PIFCN) or mesh (for the FV model).

383 Figure 9 presents the values of \mathcal{R}_h against the corresponding computational time
 384 taken to train the PICN (blue points), PIFCN (red points), and to run the FV model
 385 (green cross points) at different resolutions. The value of \mathcal{R}_h of each model is calculated
 386 from its steady-state predictions of h ; namely: $\mathcal{R}_h = \left(\sqrt{\sum (h_i - \tilde{h}_i)^2 / N_p} \right) \Big|_{t=t_s}$, where
 387 t_s is the time after which a steady state is reached for each PINN or FV model. For the
 388 computation time of FV models described in Figure 9, the value of \mathcal{T}_c is the time required
 389 for all FV models to reach steady state. The results for hu show a pattern similar to that
 390 in Figure 9 and are not presented for conciseness. All simulations achieve sub-centimetric
 391 \mathcal{R}_h , with FV (10) delivering the results at least one order of magnitude faster than the
 392 other solutions. PIFCN (10) was the slowest of all models. Figure 9 shows that the pre-
 393 diction of h from PICN (10) displays the highest accuracy, with an \mathcal{R}_h of 0.85 mm, al-
 394 though this was obtained at a computation time that was 56 times longer than FV (10).
 395 All the PINN results also attain an accuracy higher than or similar to that of FV(2). In
 396 this test case, the relative differences in the prediction accuracy among the PICN mod-
 397 els is less than the difference observed from FV (5) to FV (10). In terms of the influence
 398 of resolution on the computational speed, the PICN is also less sensitive than PIFCN
 399 in this problem.

400 3.3 Simulation of real-world river flooding

401 While Tests 1 and 2 have assessed the ability of PINN models to deal with impor-
 402 tant aspects of flow problems, such as unsteadiness and variable topography, both case
 403 studies represented idealized, one-dimensional problems. In order to investigate the per-
 404 formance of PINNs under more complex and realistic problems, this section presents the
 405 results of simulations of a real-world scenario. The scenario in question is a flood event
 406 that occurred between 27 November and 1 December 2005 in the Tiber river (Morales-
 407 Hernández et al., 2016), which flows from the Apennine Mountains to the Tyrrhenian
 408 Sea in Italy. The reach of river employed in this simulation is approximately 6 km long
 409 and is located near the city of Rome. In this region, the mean discharge of the Tiber river

410 is $267 \text{ m}^3\text{s}^{-1}$, while its peak discharge for a 200-year return period is around $3200 \text{ m}^3\text{s}^{-1}$.
 411 The event modeled in this paper was also previously simulated in Morales-Hernández
 412 et al. (2016) and Shamkhalchian and de Almeida (2021). The domain comprises an area
 413 of $6 \text{ km} \times 2 \text{ km}$. The duration of the event simulated is 113 hours. The values of Man-
 414 ning’s coefficient n used are the same as in Morales-Hernández et al. (2016) and Shamkhalchian
 415 and de Almeida (2021); namely, $n = 0.035 \text{ sm}^{-1/3}$ for the main channel, and $n = 0.0446$
 416 $\text{sm}^{-1/3}$ for the floodplains.

417 The boundary conditions were obtained from Morales-Hernández et al. (2016), and
 418 correspond to the time series of flow discharge and water surface elevation at the upstream
 419 and downstream sections of the river at the boundary of the computational domain. The
 420 initial conditions $\mathbf{U}(x, y, t = 0)$ were defined from the results of the FV model under
 421 steady-state conditions ($Q = 374 \text{ m}^3\text{s}^{-1}$) performed at 5 m resolution. PINNs were trained
 422 from datasets resolved at 50, 100 and 200 m, while the FV model was run using meshes
 423 generated from gridded data at resolutions of 10, 25 and 50 m. The corresponding tempo-
 424 ral resolution for the trainset for the PINNs is 4 hours. The batch size was set to one
 425 third of the total number of collocation points.

426 For this test case, the architecture of the PICN consists of 2 convolutional layers
 427 (the first and second layers have 10 and 40 channels, respectively) and 1 fully connected
 428 hidden layer with 100 neurons. The architecture of the PIFCN consists of 3 fully con-
 429 nected hidden layers, each having 2000 neurons. Our tests showed that further increas-
 430 ing the network complexity would not improve the model’s prediction accuracy, and may
 431 substantially increase the training time and/or cause the program to exceed the mem-
 432 ory capacity of the computer resources used.

433 Since an analytical solution is not available for this problem, the results of the FV
 434 simulation at fine resolution (5 m) were used as the benchmark. The accuracy of the so-
 435 lutions of the time-dependent variables is assessed at two cross-sections (located approx-
 436 imately at distances of $1/3$ and $2/3$ of the length of the river within the domain from
 437 the upstream boundary, and hereafter referred to as S1 and S2, respectively) at 1 hour
 438 temporal resolution.

439 Figures 10 and 11 illustrate the time series of prediction errors (right vertical axes),
 440 along with the actual predicted values of the flow depth h and flow discharge Q (left ver-
 441 tical axes) at cross-sections S1 and S2 for each PICN, PIFCN, and FV models. Figure 10
 442 shows that the FV and PIFCN simulations consistently predict larger and lower depths
 443 than the benchmark solution, respectively, at both cross sections in the main channel,
 444 while PICN results display both positive and negative values of ϵ_h . Results from PICNs
 445 at S1 and S2 are markedly more accurate than those delivered by PIFCNs and the coarse-
 446 resolution FV models. For example, FV (50) and FV (25) produced results that devi-
 447 ate substantially (i.e. up to approximately 1.2 m and 2.5 m at S1 and S2, respectively)
 448 from the benchmark solution. On the other hand, FV (10) generally produced the most
 449 accurate depth predictions out of all models tested. The ability of the models to predict
 450 flow velocities (and therefore, the volumetric flow rate Q) is assessed by $\epsilon_Q = \tilde{Q} - |Q|$,
 451 where $Q = \int h \mathbf{U} \cdot \mathbf{n} dl$ is the total discharge; l is the length along the cross-sections (i.e.,
 452 S1 and S2, which span across the whole domain) and \mathbf{n} is the unit vector normal to the
 453 cross-section. Figure 11 shows the predicted errors ϵ_Q obtained by all models as a func-
 454 tion of time. These results are markedly different from those previously presented for
 455 ϵ_h . Namely, all FV models display values of ϵ_Q that are substantially smaller than those
 456 predicted by PICN and PIFCN models. The maximum values of ϵ_Q for PICN and PIFCN
 457 are more than 50% and 70% of the benchmark (FV (5)) in S2, respectively. The pos-
 458 sible reason behind these results might be that the water surface ($\eta = h + z$) presents
 459 much less spatial variation than Q in the domain. However, this hypothesis would need
 460 to be tested thoroughly in the future through a set of specifically designed case studies.

Figure 12 assesses the overall accuracy of temporal prediction for h of each model against the corresponding computational time, using the root-mean-square error metric $\mathcal{R}_h^t = \left(\sqrt{\sum_{(x,y) \in \mathcal{S}} (h_i - \tilde{h}_i)^2 / N_p^t} \right)$, where \mathcal{S} denotes the corresponding cross-section and N_p^t is the number of collocation points in the testset. The best values of \mathcal{R}_h^t (i.e., across all epochs) obtained from all PICN models are within the range of $0.22 \text{ m} < \mathcal{R}_h^t < 0.30 \text{ m}$ (S1) and $0.26 \text{ m} < \mathcal{R}_h^t < 0.34 \text{ m}$ (S2), while FV (10) delivered $\mathcal{R}_h^t = 0.29 \text{ m}$ (S1) and 0.35 m (S2), and results from FV (25) and FV (50) were substantially less accurate. It is interesting to note that PINN models trained with coarse datasets (e.g., 200 m) do not necessarily deliver poorer accuracy compared to their fine resolution counterparts; this contrasts with what is typically observed in simulations with traditional numerical methods such as FV. Figure 12 also indicates that PICN models may offer improved depth predictions at lower cost than a FV model. For example, the accuracy of depth predictions by PICN (200) is better than the accuracy delivered by FV (10), while the computational cost is more than one order of magnitude lower. Overall, the PICN shows better h prediction performance than PIFCN and FV in terms of the speed-accuracy trade-off.

Figure 13 shows examples of flood depth maps at $t = 32$ hours obtained by the FV model at resolutions of 5 m and 25 m, along with those produced by PICN and PIFCN at 100 m resolved trainsets. As expected from the results presented in Figure 10, FV (25) overestimates h during the peak time (which also translates into a larger flooded area), while the opposite is observed for PICN (100) and PIFCN (100). Further spatial analysis can be seen in Appendix B.

4 Concluding remarks

In this paper, two physics-informed neuronal networks (PINNs) were developed to predict the evolution of free-surface flows typically modeled by the shallow water equations (SWEs). The PINN formulation eliminates the need for labeled data, which is typically required in supervised learning. This is achieved by defining a loss function that combines the SWEs, the boundary conditions (BCs) and initial conditions (ICs), allowing the trained PINN to serve as an alternative method for solving the SWEs. The two PINNs developed and tested here vary in their architecture and main features. The first is based on the fully-connected neural network (PIFCN), and the second on the convolutional neural network (PICN) approach.

Three test cases were used to assess the accuracy and computational performance of each model, including two idealized flow problems for which analytical solutions are available, and one simulation of a real-world flood event over a relatively large-scale and complex topography domain. In the idealized problems, the PICN and PIFCN predictions achieved higher accuracy (lower \mathcal{R}_h) than the Finite Volume (FV) solver employed for comparison. However, in these problems, PINNs generally took longer to reach the same prediction accuracy as the coarsely resolved FV model. For the real-world flooding problem, in general, PINNs were able to yield similarly accurate predictions of flow depths compared to finely resolved FV simulations. However, all FV models show much higher accuracy in their predictions of Q . For the spatial analysis of flow depths at the peak of the flood event, PINNs were able to produce flood maps with accuracy (relative to the benchmark finely resolved FV simulation) that is comparable to the results of FV models run at intermediate resolution (e.g., 25 m). Some of the PINN models (e.g., PICN at 100 and 200 m resolution) achieved the same level of accuracy as the 25 m resolution FV model at least one order of magnitude faster. In addition, the prediction capability of PINNs may be less affected by changes in grid resolution than the FV solver, which may represent important advantages in real-world applications where finely resolved topographic data may not always be available. At the same resolution (e.g., 10 m in Tests 1 and 2, or 50 m in Test 3), the training process of PICNs and PIFCNs with random ini-

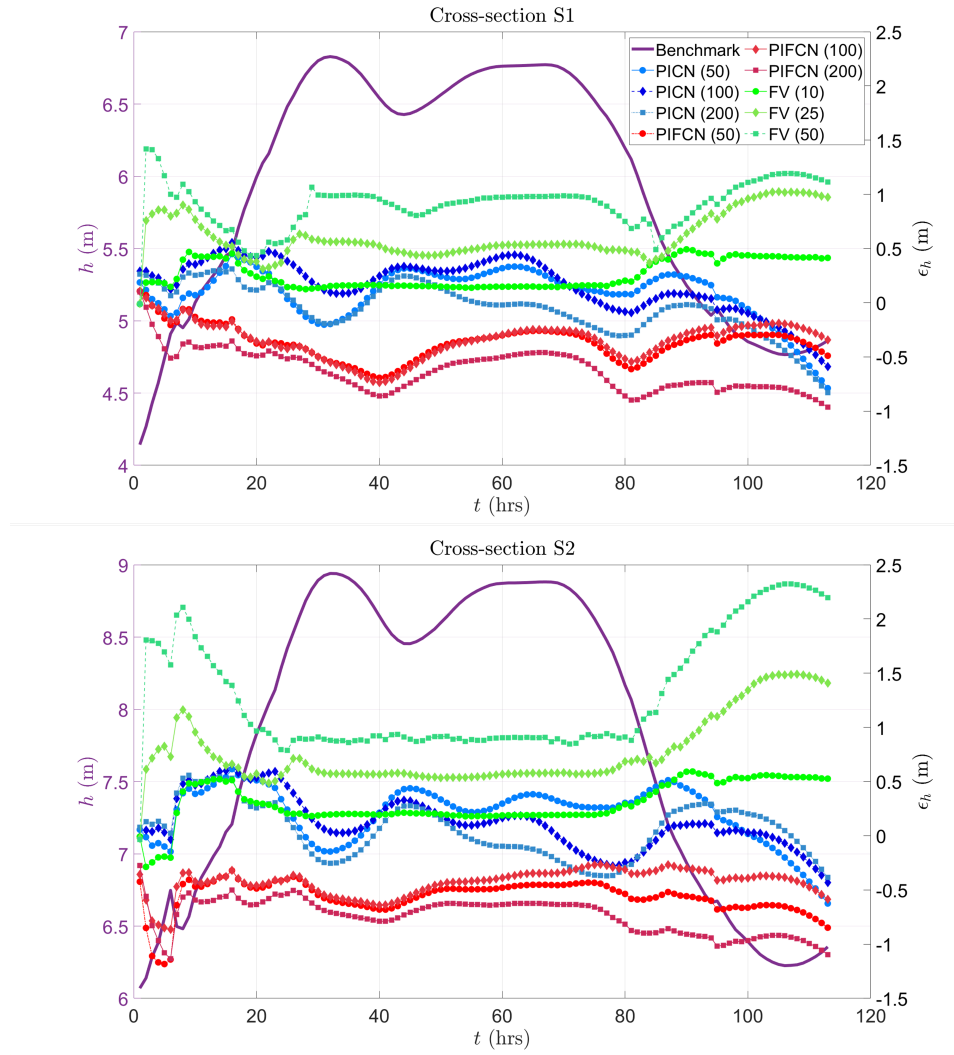


Figure 10. Test 3: Predicted water depths error ϵ_h (plotted against right y -axis) at cross-sections S1 (top) and S2 (bottom) of the main channel in the Tiber river. Benchmark solution (from a finely resolved FV simulation) shown by the purple line against the left y -axis.

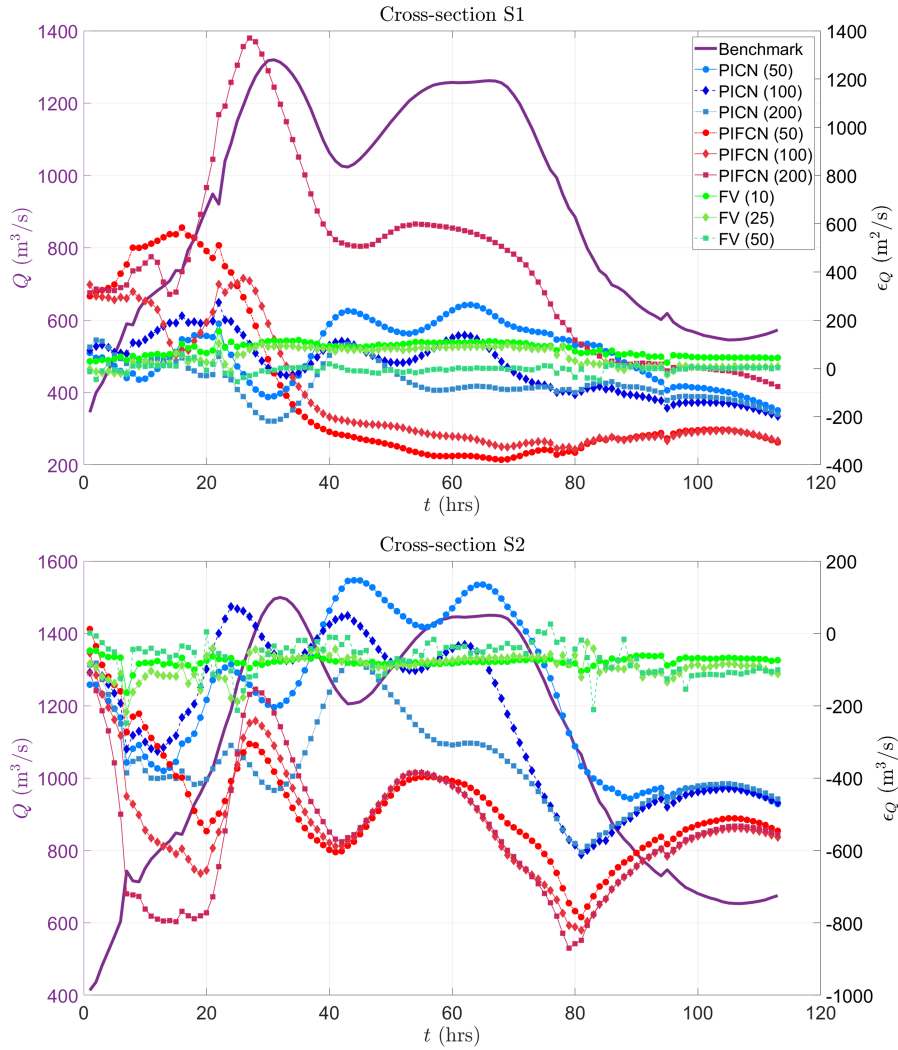


Figure 11. Test 3: Predicted water discharge error ϵ_Q (plotted against right y -axis) at cross-sections S1 (top) and S2 (bottom), which span across the whole domain. Benchmark solution (from a finely resolved FV simulation) shown by the purple line against the left y -axis.

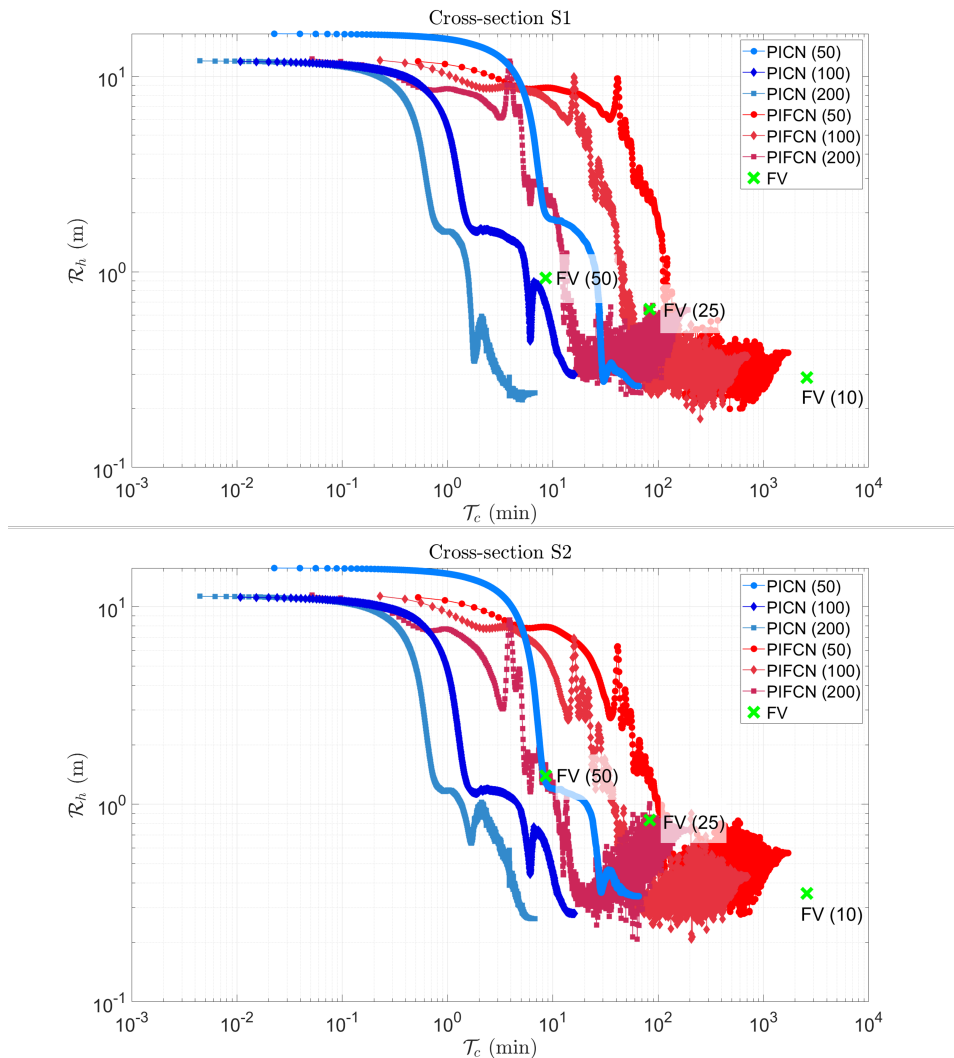


Figure 12. Test 3: \mathcal{R}_h^t as a function of \mathcal{T}_c (training time for PICN and PIFCN and run time for FV) at cross-sections S1 (top) and S2 (bottom) of the Tiber river; note that the right-most point of each cloud corresponds to the highest accuracy that any given PINN can achieve. The number in brackets represents the resolution (in meters) of the training data set (for PICN and PIFCN) or mesh (for the FV model). The benchmark results are those from the FV (5) simulation.

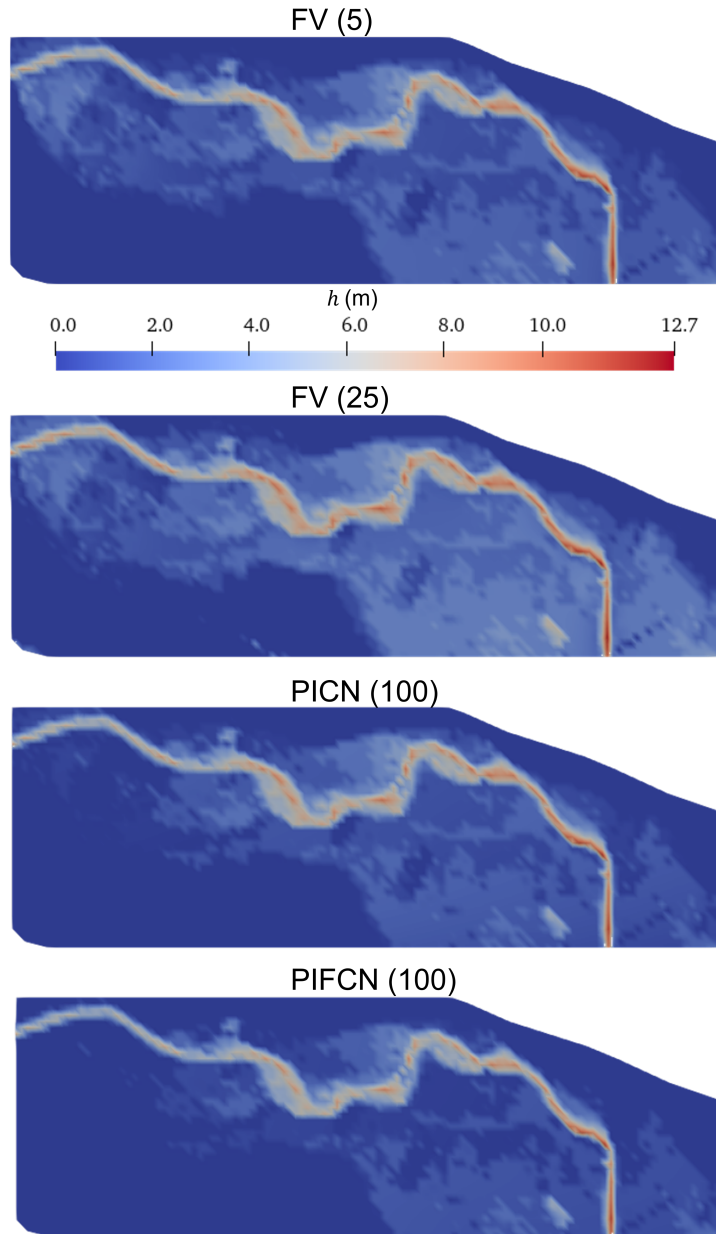


Figure 13. Examples of flood maps at time $t = 32$ hours produced by the FV model and PINNs. Note that FV (5) represents the benchmark results.

512 tialization of weights and biases takes longer than the run time of the FV model. Re-
 513 sults show that, in most circumstances, PICNs usually exhibit better performance in terms
 514 of speed-accuracy trade-off than PIFCNs. However, more comparative tests between PICN
 515 and PIFCN are necessary before reaching general conclusions in this regard.

516 While the results in this paper may not suggest that PINNs can replace other well-
 517 established numerical techniques, they indicate that PINNs (and in particular PICNs)
 518 should be considered as an emerging technique that has the potential to deliver accu-
 519 rate and efficient solutions, and which should be further developed and assessed. Our
 520 results show that the approach might be particularly useful under certain circumstances
 521 which are challenging to conventional techniques. For example, in simulations performed
 522 at coarse resolutions (a typical case in real-world problems), PINN models may achieve
 523 a higher prediction accuracy with a lower computational cost than a FV solver. Since
 524 these techniques are still in their infancy, further research and development may enable
 525 PINNs to become a competitive alternative to simulate flow problems governed by the
 526 SWEs in the near future.

527 5 Open Research

528 The simulation data used for all three test cases in the study are available at the
 529 database from University of Southampton via <https://doi.org/10.5258/SOTON/D2645>
 530 with CC-BY license (Xin Qi, 2023).

531 Acknowledgments

532 The authors acknowledge the use of the IRIDIS High Performance Computing Facility,
 533 and associated support services at the University of Southampton, in the completion of
 534 this work.

535 References

- 536 Alcrudo, F., & Garcia-Navarro, P. (1993). A high-resolution godunov-type scheme
 537 in finite volumes for the 2d shallow-water equations. *International Journal for*
 538 *Numerical Methods in Fluids*, 16(6), 489–505.
- 539 Bale, D. S., Leveque, R. J., Mitran, S., & Rossmanith, J. A. (2003). A wave prop-
 540 agation method for conservation laws and balance laws with spatially varying
 541 flux functions. *SIAM Journal on Scientific Computing*, 24(3), 955–978.
- 542 Baydin, A. G., Pearlmutter, B. A., Radul, A. A., & Siskind, J. M. (2018). Au-
 543 tomatic differentiation in machine learning: a survey. *Journal of Machine*
 544 *Learning Research*, 18, 1–43.
- 545 Bermúdez, M., Cea, L., & Puertas, J. (2019). A rapid flood inundation model for
 546 hazard mapping based on least squares support vector machine regression.
 547 *Journal of Flood Risk Management*, 12(August 2018), 1–14. (Times cited: 6
 548 Flooding papers) doi: 10.1111/jfr3.12522
- 549 Bernard, P.-E., Remacle, J.-F., Comblen, R., Legat, V., & Hillewaert, K. (2009).
 550 High-order discontinuous galerkin schemes on general 2d manifolds applied
 551 to the shallow water equations. *Journal of Computational Physics*, 228(17),
 552 6514–6535.
- 553 Bihlo, A., & Popovych, R. O. (2022). Physics-informed neural networks for the
 554 shallow-water equations on the sphere. *Journal of Computational Physics*, 456,
 555 111024. doi: <https://doi.org/10.1016/j.jcp.2022.111024>
- 556 Blumer, A., Ehrenfeucht, A., Haussler, D., & Warmuth, M. K. (1987). Occam’s raz-
 557 or. *Information Processing Letters*, 24(6), 377–380. doi: [https://doi.org/10](https://doi.org/10.1016/0020-0190(87)90114-1)
 558 [.1016/0020-0190\(87\)90114-1](https://doi.org/10.1016/0020-0190(87)90114-1)
- 559 Botta, N., Klein, R., Langenberg, S., & Lützenkirchen, S. (2004). Well balanced

- 560 finite volume methods for nearly hydrostatic flows. *Journal of Computational*
561 *Physics*, 196(2), 539–565.
- 562 Cai, S., Wang, Z., Wang, S., Perdikaris, P., & Karniadakis, G. E. (2021). Physics-
563 informed neural networks for heat transfer problems. *Journal of Heat Transfer*,
564 143(6).
- 565 Carbonneau, R., Laframboise, K., & Vahidov, R. (2008). Application of machine
566 learning techniques for supply chain demand forecasting. *European Journal of*
567 *Operational Research*, 184(3), 1140–1154.
- 568 Casulli, V. (1990). Semi-implicit finite difference methods for the two-dimensional
569 shallow water equations. *Journal of Computational Physics*, 86(1), 56–74.
- 570 Dawson, C., Westerink, J. J., Feyen, J. C., & Pothina, D. (2006). Continuous,
571 discontinuous and coupled discontinuous–continuous galerkin finite element
572 methods for the shallow water equations. *International Journal for Numerical*
573 *Methods in Fluids*, 52(1), 63–88.
- 574 de Almeida, G. A., & Bates, P. (2013). Applicability of the local inertial approxi-
575 mation of the shallow water equations to flood modeling. *Water Resources Re-*
576 *search*, 49(8), 4833–4844.
- 577 de Almeida, G. A., Bates, P., & Ozdemir, H. (2016). Modelling urban floods at sub-
578 metre resolution: challenges or opportunities for flood risk management? *Jour-*
579 *nal of Flood Risk Management*, 11, S855–S865.
- 580 Delestre, O., Lucas, C., Ksinant, P.-A., Darboux, F., Laguerre, C., Vo, T.-N.-T.,
581 ... Cordier, S. (2013). SWASHES: a compilation of shallow water analytic
582 solutions for hydraulic and environmental studies. *International Journal for*
583 *Numerical Methods in Fluids*, 72(3), 269–300. doi: 10.1002/fld.3741
- 584 El Naqa, I., Li, R., & Murphy, M. J. (2015). *Machine learning in radiation oncology:*
585 *theory and applications*. Springer.
- 586 Ferrari, A., & Vacondio, R. (2022). An augmented hlem ader numerical model par-
587 allel on gpu for the porous shallow water equations. *Computers & Fluids*, 238,
588 105360.
- 589 Gao, H., Sun, L., & Wang, J.-X. (2021). Phygeonet: Physics-informed geometry-
590 adaptive convolutional neural networks for solving parameterized steady-state
591 pdes on irregular domain. *Journal of Computational Physics*, 428, 110079.
- 592 Guo, L., Ye, S., Han, J., Zheng, H., Gao, H., Chen, D. Z., ... Wang, C. (2020). Ssr-
593 vfd: Spatial super-resolution for vector field data analysis and visualization. In
594 2020 *ieee pacific visualization symposium (pacificvis)* (p. 71-80). doi: 10.1109/
595 PacificVis48177.2020.8737
- 596 Haghghat, E., Raissi, M., Moure, A., Gomez, H., & Juanes, R. (2020). A deep
597 learning framework for solution and discovery in solid mechanics. *arXiv*
598 *preprint arXiv:2003.02751*.
- 599 Hanert, E., Le Roux, D. Y., Legat, V., & Deleersnijder, E. (2005). An efficient eu-
600 lerian finite element method for the shallow water equations. *Ocean Modelling*,
601 10(1-2), 115–136.
- 602 Haykin, S. (2009). *Neural networks and learning machines* (Third Edit ed.). Upper
603 Saddle River: Prentice-Hall.
- 604 Henrique, B. M., Sobreiro, V. A., & Kimura, H. (2019). Literature review: Machine
605 learning techniques applied to financial market prediction. *Expert Systems with*
606 *Applications*, 124, 226–251.
- 607 Hornik, K., Stinchcombe, M., & White, H. (1989). Multilayer feedforward networks
608 are universal approximators. *Neural networks*, 2(5), 359–366.
- 609 Hunter, N. M., Horritt, M. S., Bates, P. D., Wilson, M. D., & Werner, M. G. (2005).
610 An adaptive time step solution for raster-based storage cell modelling of flood-
611 plain inundation. *Advances in water resources*, 28(9), 975–991.
- 612 Ioffe, S., & Szegedy, C. (2015). Batch normalization: Accelerating deep network
613 training by reducing internal covariate shift. *CoRR*, abs/1502.03167.
- 614 Jin, X., Cai, S., Li, H., & Karniadakis, G. E. (2021). Nsfnets (navier-stokes flow

- 615 nets): Physics-informed neural networks for the incompressible navier-stokes
 616 equations. *Journal of Computational Physics*, *426*, 109951.
- 617 Juez, C., Murillo, J., & García-Navarro, P. (2014). A 2d weakly-coupled and efficient
 618 numerical model for transient shallow flow and movable bed. *Advances in Wa-*
 619 *ter Resources*, *71*, 93–109.
- 620 Kabir, S., Patidar, S., Xia, X., Liang, Q., Neal, J., & Pender, G. (2020). A deep
 621 convolutional neural network model for rapid prediction of fluvial flood inunda-
 622 tion. *Journal of Hydrology*, *590*, 125481.
- 623 Khan, S., & Yairi, T. (2018). A review on the application of deep learning in system
 624 health management. *Mechanical Systems and Signal Processing*, *107*, 241–265.
- 625 Kingma, D. P., & Ba, J. (2014). Adam: A method for stochastic optimization. *arXiv*
 626 *preprint arXiv:1412.6980*.
- 627 Krishnapriyan, A., Gholami, A., Zhe, S., Kirby, R., & Mahoney, M. W. (2021).
 628 Characterizing possible failure modes in physics-informed neural networks.
 629 *Advances in Neural Information Processing Systems*, *34*.
- 630 Kurganov, A., & Levy, D. (2002). Central-upwind schemes for the saint-venant
 631 system. *ESAIM: Mathematical Modelling and Numerical Analysis*, *36*(3), 397–
 632 425.
- 633 Leandro, J., Chen, A., & Schumann, A. (2014). A 2d parallel diffusive wave model
 634 for floodplain inundation with variable time step (p-dwave). *Journal of Hydrol-*
 635 *ogy*, *517*, 250–259.
- 636 Leskens, J., Brugnach, M., Hoekstra, A. Y., & Schuurmans, W. (2014). Why are
 637 decisions in flood disaster management so poorly supported by information
 638 from flood models? *Environmental modelling & software*, *53*, 53–61.
- 639 LeVeque, R. J., George, D. L., & Berger, M. J. (2011). Tsunami modelling with
 640 adaptively refined finite volume methods. *Acta Numerica*, *20*, 211–289.
- 641 Li, C., Han, Z., Li, Y., Li, M., Wang, W., Dou, J., ... Chen, G. (2023). Physical
 642 information-fused deep learning model ensembled with a subregion-specific
 643 sampling method for predicting flood dynamics. *Journal of Hydrology*, *620*,
 644 129465. Retrieved from <https://www.sciencedirect.com/science/article/pii/S0022169423004079> doi: <https://doi.org/10.1016/j.jhydrol.2023.129465>
- 645 Li, J., Cao, Z., & Borthwick, A. G. (2022). Quantifying multiple uncertainties
 646 in modelling shallow water-sediment flows: A stochastic galerkin frame-
 647 work with haar wavelet expansion and an operator-splitting approach. *Ap-*
 648 *plied Mathematical Modelling*, *106*, 259-275. Retrieved from [https://](https://www.sciencedirect.com/science/article/pii/S0307904X22000579)
 649 www.sciencedirect.com/science/article/pii/S0307904X22000579 doi:
 650 <https://doi.org/10.1016/j.apm.2022.01.032>
- 651 Li, R., Lee, E., & Luo, T. (2021). Physics-informed neural networks for solving mul-
 652 tiscala mode-resolved phonon boltzmann transport equation. *Materials Today*
 653 *Physics*, *19*, 100429.
- 654 Liang, Q. (2011). A structured but non-uniform cartesian grid-based model for the
 655 shallow water equations. *International Journal for Numerical Methods in Flu-*
 656 *ids*, *66*(5), 537–554.
- 657 Liang, Q., & Marche, F. (2009). Numerical resolution of well-balanced shallow wa-
 658 ter equations with complex source terms. *Advances in water resources*, *32*(6),
 659 873–884.
- 660 Liu, Y., & Pender, G. (2015). A flood inundation modelling using v-support vector
 661 machine regression model. *Engineering Applications of Artificial Intelligence*,
 662 *46*, 223–231. (Times cited: 4 Flooding papers) doi: 10.1016/j.engappai.2015.09
 663 .014
- 664 Lynch, D. R., & Gray, W. G. (1979). A wave equation model for finite element tidal
 665 computations. *Computers & fluids*, *7*(3), 207–228.
- 666 MacDonald, I. (1996). *Analysis and computation of steady open channel flow* (Un-
 667 published doctoral dissertation). Citeseer.
- 668 Mahesh, R. B., Leandro, J., & Lin, Q. (2022). Physics informed neural network for
 669

- 670 spatial-temporal flood forecasting. In *Climate change and water security* (pp.
671 77–91). Springer.
- 672 Mao, Z., Jagtap, A. D., & Karniadakis, G. E. (2020). Physics-informed neural net-
673 works for high-speed flows. *Computer Methods in Applied Mechanics and Engi-
674 neering*, *360*, 112789.
- 675 Marras, S., Kelly, J. F., Moragues, M., Müller, A., Kopera, M. A., Vázquez, M., ...
676 Jorba, O. (2016). A review of element-based galerkin methods for numerical
677 weather prediction: Finite elements, spectral elements, and discontinuous
678 galerkin. *Archives of Computational Methods in Engineering*, *23*(4), 673–722.
- 679 Molls, T., & Chaudhry, M. H. (1995). Depth-averaged open-channel flow model.
680 *Journal of Hydraulic Engineering*, *121*(6), 453–465.
- 681 Monnier, J., Couderc, F., Dartus, D., Larnier, K., Madec, R., & Vila, J.-P. (2016).
682 Inverse algorithms for 2d shallow water equations in presence of wet dry fronts:
683 Application to flood plain dynamics. *Advances in Water Resources*, *97*, 11–
684 24.
- 685 Morales-Hernández, M., Petaccia, G., Brufau, P., & García-Navarro, P. (2016).
686 Conservative 1d–2d coupled numerical strategies applied to river flooding: The
687 tiber (rome). *Applied Mathematical Modelling*, *40*(3), 2087–2105.
- 688 Pang, G., Lu, L., & Karniadakis, G. E. (2019). fpinns: Fractional physics-informed
689 neural networks. *SIAM Journal on Scientific Computing*, *41*(4), A2603–
690 A2626.
- 691 Paszke, A., Gross, S., Chintala, S., Chanan, G., Yang, E., DeVito, Z., ... Lerer, A.
692 (2017). Automatic differentiation in pytorch.
- 693 Raissi, M., Perdikaris, P., & Karniadakis, G. E. (2019). Physics-informed neural
694 networks: A deep learning framework for solving forward and inverse problems
695 involving nonlinear partial differential equations. *Journal of Computational
696 Physics*, *378*, 686–707.
- 697 Rastgoo, R., Kiani, K., Escalera, S., & Sabokrou, M. (2021). Sign language pro-
698 duction: A review. In *Proceedings of the ieee/cvf conference on computer vi-
699 sion and pattern recognition* (pp. 3451–3461).
- 700 Sanders, B. F., & Schubert, J. E. (2019). Primo: Parallel raster inundation model.
701 *Advances in Water Resources*, *126*, 79–95.
- 702 Shamkhalchian, A., & de Almeida, G. A. (2021). Upscaling the shallow water equa-
703 tions for fast flood modelling. *Journal of Hydraulic Research*, *59*(5), 739–756.
- 704 Smith, L. N., & Topin, N. (2019). Super-convergence: Very fast training of neu-
705 ral networks using large learning rates. In *Artificial intelligence and machine
706 learning for multi-domain operations applications* (Vol. 11006, p. 1100612).
- 707 Ștefănescu, R., Sandu, A., & Navon, I. M. (2014). Comparison of pod reduced or-
708 der strategies for the nonlinear 2d shallow water equations. *International Jour-
709 nal for Numerical Methods in Fluids*, *76*(8), 497–521.
- 710 Sulavko, A. (2020). Bayes-minkowski measure and building on its basis immune
711 machine learning algorithms for biometric facial identification. In *Journal of
712 physics: Conference series* (Vol. 1546, p. 012103).
- 713 Sun, L., Gao, H., Pan, S., & Wang, J.-X. (2020). Surrogate modeling for fluid flows
714 based on physics-constrained deep learning without simulation data. *Computer
715 Methods in Applied Mechanics and Engineering*, *361*, 112732.
- 716 Toro, E. F., & Garcia-Navarro, P. (2007). Godunov-type methods for free-surface
717 shallow flows: A review. *Journal of Hydraulic Research*, *45*(6), 736–751.
- 718 Vlassis, N. N., & Sun, W. (2021). Sobolev training of thermodynamic-informed neu-
719 ral networks for interpretable elasto-plasticity models with level set hardening.
720 *Computer Methods in Applied Mechanics and Engineering*, *377*, 113695.
- 721 Voulodimos, A., Doulamis, N., Doulamis, A., & Protopapadakis, E. (2018). Deep
722 learning for computer vision: A brief review. *Computational intelligence and
723 neuroscience*, *2018*.
- 724 William, W., Ware, A., Basaza-Ejiri, A. H., & Obungoloch, J. (2018). A review of

- 725 image analysis and machine learning techniques for automated cervical cancer
726 screening from pap-smear images. *Computer methods and programs in*
727 *biomedicine*, 164, 15–22.
- 728 Wilson, M., Bates, P., Alsdorf, D., Forsberg, B., Horritt, M., Melack, J., ... Famigli-
729 etti, J. (2007). Modeling large-scale inundation of amazonian seasonally
730 flooded wetlands. *Geophysical Research Letters*, 34(15).
- 731 Xin Qi, S. M., Gustavo A. M. de Almeida. (2023). *Dataset supporting an article*
732 *"physics informed neural networks for solving flow problems modeled by the*
733 *shallow water equations"* [dataset]. University of Southampton. Retrieved
734 from <https://doi.org/10.5258/SOTON/D2645> doi: 10.5258/SOTON/D2645
- 735 Yıldız, S., Goyal, P., Benner, P., & Karasözen, B. (2021). Learning reduced-order
736 dynamics for parametrized shallow water equations from data. *International*
737 *Journal for Numerical Methods in Fluids*, 93(8), 2803–2821.
- 738 Yoon, T. H., & Kang, S.-K. (2004). Finite volume model for two-dimensional shal-
739 low water flows on unstructured grids. *Journal of Hydraulic Engineering*,
740 130(7), 678–688.
- 741 Zhang, R., Liu, Y., & Sun, H. (2020). Physics-guided convolutional neural network
742 (phycnn) for data-driven seismic response modeling. *Engineering Structures*,
743 215, 110704.
- 744 Zhu, X. X., Tuia, D., Mou, L., Xia, G.-S., Zhang, L., Xu, F., & Fraundorfer, F.
745 (2017). Deep learning in remote sensing: A comprehensive review and list of
746 resources. *IEEE Geoscience and Remote Sensing Magazine*, 5(4), 8–36.
- 747 Zhu, Y., Zabararas, N., Koutsourelakis, P.-S., & Perdikaris, P. (2019). Physics-
748 constrained deep learning for high-dimensional surrogate modeling and uncer-
749 tainty quantification without labeled data. *Journal of Computational Physics*,
750 394, 56–81.

Appendix A PINN Design Experiments

This section illustrates the heuristic approach followed to determine the best possible design of the PINNs. We focus on Test 1, described in Section 3.1. All the PINNs shown in this section are trained from the same dataset resolved at 50 m resolution. Figures A1 and A2 show the accuracy (\mathcal{R}_h) of the PICNs and PIFCNs, respectively, as their architecture (number of layers and channels/neurons) is varied. In short, these figures show that it is difficult to conclude whether a single architecture can lead to significantly improved results, and we thus prioritize simplicity in our PINNs design. While this heuristic approach is, by definition, not guaranteed to find the optimal solution, it represents the summary of very many iterations. This holds for other tests and dataset resolutions considered in this study.

Similarly, we have tested three widely used activation functions: Relu, Sigmoid and Tanh (see Table A1). The chosen architecture for testing the PICN and PIFCN models is CNN-5-20 and FCNN-3(1000), respectively. For PICN, Sigmoid and Tanh display the same accuracy, while the result of the Relu-based PICN has higher errors. The PIFCN with Tanh yields better accuracy than using the other two activation functions. As a result, Tanh was chosen as the activation function to be employed in all PINNs discussed in this paper.

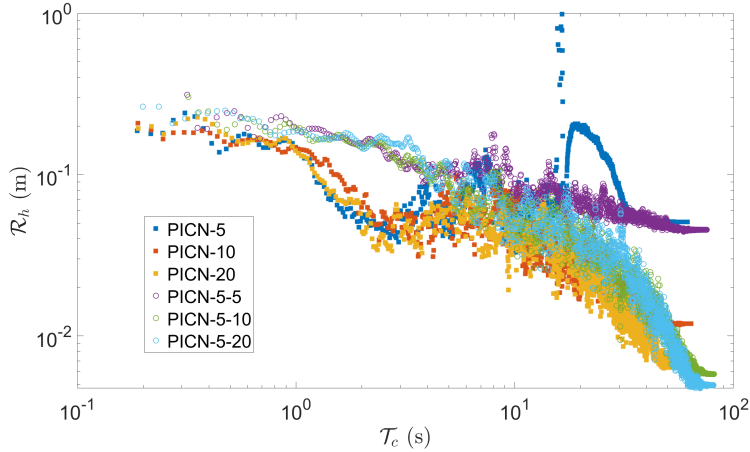


Figure A1. Comparison of PICNs with different architectures; the last hidden layer of all PICNs is one typical fully connected layer with 50 neurons. In the legend bar, the following format is adopted: PICN-X-Y, where the PICN has X channels in the first convolutional layer and Y channels in the second convolutional layer (thus, PICN-X denotes a network with one convolutional layer only).

Table A1. Results of water depth prediction by using Relu, Sigmoid and Tanh activation functions for PICN and PIFCN models. The trainset is a 50 m resolved dataset from Test 1; the evaluation metric is \mathcal{R}_h and its unit is m.

Model	Relu	Sigmoid	Tanh
PICN	0.021	0.002	0.002
PIFCN	0.154	0.028	0.004

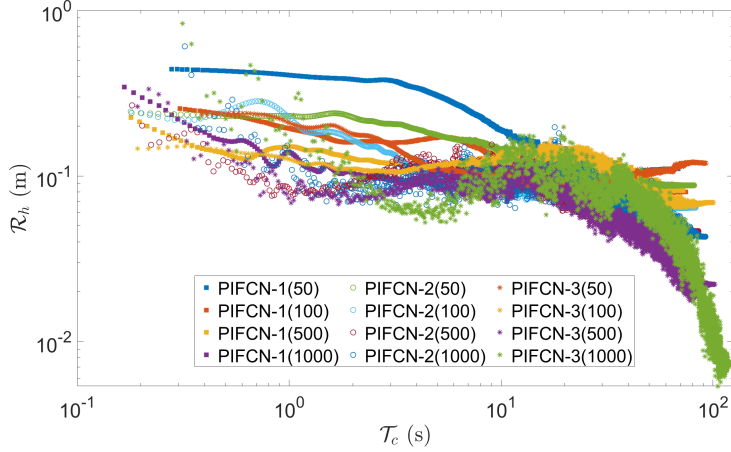


Figure A2. Comparison of PIFCNs with different architectures. In the legend bar, the following format is adopted: PIFCN-X(Y), where X denotes the number of hidden layers and Y is the number of neurons per layer.

769

Appendix B Further Spatial Analysis For Test 3

Table B1. Computation time and spatial prediction accuracy relative to benchmark simulation for the comparison. The unit for \mathcal{R}_h^s is m, and the unit for \mathcal{R}_{hu}^s and \mathcal{R}_{hv}^s is m^2s^{-1} .

Model name	\mathcal{T}_c (min)	t = 32 hours			t = 68 hours		
		\mathcal{R}_h^s	\mathcal{R}_{hu}^s	\mathcal{R}_{hv}^s	\mathcal{R}_h^s	\mathcal{R}_{hu}^s	\mathcal{R}_{hv}^s
PICN (50)	59.4	0.52	1.68	1.16	0.41	1.87	1.21
PICN (100)	15.3	0.40	1.72	1.18	0.37	1.92	1.20
PICN (200)	5.3	0.48	1.69	1.12	0.39	1.88	1.17
PIFCN (50)	504.9	0.59	2.21	1.32	0.52	2.21	1.28
PIFCN (100)	127.9	0.59	2.16	1.28	0.50	2.21	1.18
PIFCN (200)	30.2	0.63	2.27	1.21	0.47	2.16	1.15
FV (10)	2576.0	0.19	0.89	0.56	0.19	0.86	0.56
FV (25)	83.3	0.64	1.20	1.25	0.64	1.36	1.21
FV (50)	8.6	1.24	2.18	1.95	1.24	2.32	1.87

770

771

772

773

774

775

776

777

778

779

780

Table B1 summarizes the spatial prediction accuracy (i.e. \mathcal{R}_h^s , \mathcal{R}_{hu}^s , \mathcal{R}_{hv}^s) computed from a 50 m resolved set of points for each model at $t = 32$ and 68 hours, as well as their overall \mathcal{T}_c (i.e. training time for PINN and computation time for FV). Among all the models, FV (10) and FV (50) achieve the highest and lowest accuracy, respectively. All PINNs present lower \mathcal{R}_h^s than FV (25) and FV (50). On the other hand, FV (25) is more accurate than all PINNs in terms of hu prediction. PIFCN show a relatively similar value of \mathcal{R}_{hu}^s to FV (50) at both time points. Moreover, the prediction accuracy of the PICNs and PIFCNs is less affected by the resolution of the input dataset than in the FV model. This last point may potentially be a main advantage of PINNs relative to conventional numerical methods in general, whose performance (numerical stability and accuracy) tends to be highly dependent on the mesh resolution.

Abstract

This paper investigates the application of physics-informed neural networks (PINNs) to solve free-surface flow problems governed by the two-dimensional shallow water equations (SWEs). Two types of PINNs are developed and analysed: a physics-informed fully connected neural network (PIFCN) and a physics-informed convolutional neural network (PICN). The PINNs eliminate the need for labelled data for training by employing the SWEs, initial and boundary conditions as components of the loss function to be minimized. Solutions obtained by both PINNs are compared against those delivered by a finite volume (FV) solver for two idealized problems admitting analytical solutions, and one real-world flood event. The results of these tests show that the prediction accuracy and computation time (i.e., training time) of both PINNs may be less affected by the resolution of the domain discretization than the FV model. Overall, the PICN shows a better trade-off between computational speed and accuracy than the PIFCN. Also, our results for the two idealized problems indicated that PICN and PIFCN can provide more accurate predictions than the FV model, while the FV simulation with coarse resolution (e.g., 5 m and 10 m) outperformed PICN and PIFCN in terms of the speed-accuracy trade-off. Results from the real-world test showed the finely resolved (10 m resolution) FV simulation generally provided the most accurate approximations at flooding peaks. However, both PINNs showed better speed-accuracy trade-off than the FV model in terms of predicting the temporal distribution of water depth, while FV models outperformed the PINNs in their predictions of discharge.

1 Introduction

Free-surface flow phenomena are usually modeled by the shallow water equations (SWEs), a nonlinear system of partial differential equations (PDEs) governing the evolution of water depth and vertically averaged velocity in the two horizontal dimensions. Over the last decades, significant efforts have been made to approximate the solution to the SWEs in a discretized form through numerical methods, such as Finite Difference (FD) (e.g., Casulli, 1990; Molls & Chaudhry, 1995; Kurganov & Levy, 2002, and others), Finite Volume (FV) (e.g., Alcrudo & Garcia-Navarro, 1993; Bale et al., 2003; Botta et al., 2004; Yoon & Kang, 2004; Toro & Garcia-Navarro, 2007, and others), or Finite Element (FE) (e.g., Lynch & Gray, 1979; Hanert et al., 2005; Dawson et al., 2006; Marras et al., 2016, and others). These methods are now well-established and have been the object of extensive tests and validation (e.g., Toro & Garcia-Navarro, 2007; Wilson et al., 2007; Liang & Marche, 2009; LeVeque et al., 2011, and others). While the ability of these models to capture the main properties of free-surface flows has been widely verified, accurate solutions to real-world problems typically require the use of a finely resolved computational mesh, which tends to significantly increase the computational cost (Bernard et al., 2009; Liang, 2011; Juez et al., 2014). In explicit schemes for the solution of the 2D SWEs, the computational cost C scales cubically with the size of the computational grid Δx (i.e., $C \sim \Delta x^{-3}$). As a result, important applications such as large-scale flood simulations are often beyond the capabilities of available numerical methods given existing computational resources. This is particularly challenging when simulations need to be performed in real-time, or as part of a probabilistic flood risk analysis (Leskens et al., 2014; Sanders & Schubert, 2019; Ferrari & Vacondio, 2022; J. Li et al., 2022). For example, flood risk management usually requires the simulation of a large number of inundation scenarios, which may increase the overall computational time by orders of magnitude. Although the computational speed of models can be improved by using state-of-the-art hardware and parallel computing algorithms (Leandro et al., 2014; Monnier et al., 2016), such techniques may still be insufficient to meet the computational requirements of many important applications (Kabir et al., 2020). Owing to these limitations, a cost-effective model for free-surface problems may offer an appealing alternative.

63 Over the last decades, Machine Learning (ML) models, and Artificial Neural Net-
64 works (ANNs) in particular, have found a wide range of applications, such as in finan-
65 cial prediction (Henrique et al., 2019), facial recognition (Sulavko, 2020), supply chain
66 optimization (Carbonneau et al., 2008), radiation forecasting (El Naqa et al., 2015), and
67 automatic cancer screening (William et al., 2018), to cite only a few. The extraordinary
68 increase in applications of ML models is largely due to their ability to mathematically
69 describe any nonlinear relationship between inputs and outputs according to the univer-
70 sal approximation theorem (Hornik et al., 1989), the increasing availability of data for
71 training, and increasing computational power.

72 The first works using ML for the solution of problems governed by the SWEs are
73 relatively recent and focused on the development of simple meta-models (e.g., Kabir et
74 al., 2020; Liu & Pender, 2015; Bermúdez et al., 2019; Mahesh et al., 2022, and others).
75 In this type of model, ML is used to build a prediction model to describe the input-output
76 relationship previously obtained through the solution of the governing PDEs by another
77 numerical approximation model; i.e. the ML model thus becomes a surrogate model. These
78 surrogate models typically need to be trained using the results of a large number of nu-
79 merical simulations conducted at fine resolution, which can be very computationally de-
80 manding.

81 Physics-Informed Neural Networks (PINNs), for which data (and therefore expen-
82 sive numerical simulations) are not required for training, have gained increasing atten-
83 tion in recent years (Pang et al., 2019; Mao et al., 2020; Cai et al., 2021; Krishnapriyan
84 et al., 2021; Jin et al., 2021). A PINN is essentially a ML algorithm which uses the in-
85 formation contained in the physical laws (such as the governing PDEs, boundary and
86 initial conditions) to train the model. This eliminates the need for training data and thus,
87 expensive numerical simulations. A data-free PINN is required to satisfy the governing
88 PDEs, Initial Conditions (ICs) and Boundary Conditions (BCs) simultaneously. Recent
89 applications of ML algorithms to solve complex physics phenomena have focused on the
90 use of Deep Learning (DL) models (e.g., Sun et al., 2020; Zhang et al., 2020; Haghghat
91 et al., 2020; Vlassis & Sun, 2021, and others). DL is a form of ANN with more than one
92 hidden layer, which provides the complexity required to model intricate nonlinear rela-
93 tionships, such as those found in computer vision (Voulodimos et al., 2018), health man-
94 agement (Khan & Yairi, 2018), language translation (Rastgoo et al., 2021), and remote
95 sensing (X. X. Zhu et al., 2017). In the past few years, a large number of data-free PINNs
96 have been developed by employing DL techniques, such as the Fully Connected Neural
97 Networks (FCNNs) and Convolutional Neural Networks (CNNs). For example, in Raissi
98 et al. (2019) several FCNNs were trained to predict the solutions to various systems of
99 PDEs, including Allen–Cahn, Schrödinger, Navier–Stokes, and Korteweg–de Vries equa-
100 tions. In the context of fluid dynamics, other implementations of FCNNs include those
101 of Sun et al. (2020) and Mao et al. (2020), who used their DL models to find solutions
102 to the Navier–Stokes (in steady state) and Euler equations (involving shock waves), re-
103 spectively. The use of CNNs has also been explored, for instance, for problems governed
104 by the Navier–Stokes (Cai et al., 2021) and Boltzmann transport equations (R. Li et al.,
105 2021), or for predicting steady flow in random heterogeneous media (Y. Zhu et al., 2019).
106 The success of these works shows that data-free PINNs should be considered as serious
107 contenders for solving flow problems that are typically modelled by PDEs, and which
108 have been traditionally solved using conventional numerical methods (FD, FV, etc.).

109 While ML trained from labeled data (i.e., mainly conventional numerical solutions)
110 has been used to solve the SWEs (e.g., Mahesh et al., 2022; Ștefănescu et al., 2014; Yıldız
111 et al., 2021; C. Li et al., 2023, and others), to the authors’ knowledge only a very lim-
112 ited number of articles (e.g., Bihlo & Popovych, 2022) has been published so far on the
113 use of a data-free PINNs for this purpose. In Bihlo and Popovych (2022), a PINN (specif-
114 ically, based on a FCNN) was employed to find solutions to the SWEs on a spherical do-
115 main, and the focus was on idealized problems which may find applications in meteo-

116 rology. Whether a similar DL technique may be used to accurately and efficiently solve
 117 challenging free-surface flow problems involving friction and complex boundary condi-
 118 tions, such as large-scale simulations of flow over complex topography in rivers and coastal
 119 areas, remains an open question.

120 The solution of PDEs, and in particular of the SWEs, using PINN algorithms is
 121 still in its infancy and further investigation is required to understand the main charac-
 122 teristics of solutions obtained by these methods. Firstly, the trainset for PINNs needs
 123 to be generated from a particular, discrete, set of points. It remains unclear how accu-
 124 racy and computational performance (i.e., training speed) depend on the discretization
 125 of the domain. Additionally, both FCNNs and CNNs are commonly used DL models in
 126 the research field of PINN. However, in a specific problem governed by a system of PDEs,
 127 it is usually difficult to determine which one will deliver the best performance before car-
 128 rying out tests.

129 The aim of this paper is to develop and test two different PINN models to approx-
 130 imate solutions to various free-surface flow problems governed by the 2D SWEs. The PINN
 131 models are based on the FCNN and CNN approaches, and are hereafter referred to as
 132 PIFCN (physics informed fully connected network) and PICN (physics informed convo-
 133 lutional network), respectively. These models are data-free in that they do not require
 134 data from separate numerical simulations, or laboratory/field measurements, to train the
 135 networks. In this paper both PIFCNs and PICNs are compared against the Finite Vol-
 136 ume (FV) solver of the 2D SWE developed by de Almeida et al. (2016) through a set
 137 of test cases including two idealized flow problems and one real-world flood event. The
 138 rest of this paper is organized as follows. First, the governing equations and the frame-
 139 work of both PINNs are described in Section 2. This section also provides a concise re-
 140 view of FCNNs and CNNs. In Section 3, the accuracy and computational performance
 141 of the proposed physics-informed networks (PIFCN and PICN) are investigated for the
 142 three test cases. The main outcomes of the study are discussed and summarized in Sec-
 143 tion 4.

144 2 Methods

145 2.1 Overview

146 Most problems requiring the simulation of free-surface flows in the horizontal plane,
 147 such as flow in rivers and estuaries, dam-breaks, and flood wave propagation can be mod-
 148 eled by the SWEs. The 2D SWEs represent a system of nonlinear, hyperbolic PDEs de-
 149 scribing the conservation of water mass and depth-average momentum, which can be ex-
 150 pressed as:

$$\frac{\partial \mathbf{U}}{\partial t} + \frac{\partial \mathbf{F}(\mathbf{U})}{\partial x} + \frac{\partial \mathbf{G}(\mathbf{U})}{\partial y} = \mathbf{S}(\mathbf{U}); \quad (1)$$

$$\mathbf{U} = \begin{bmatrix} h \\ hu \\ hv \end{bmatrix}, \quad \mathbf{F}(\mathbf{U}) = \begin{bmatrix} hu \\ hu^2 + \frac{1}{2}gh^2 \\ huv \end{bmatrix}, \quad \mathbf{G}(\mathbf{U}) = \begin{bmatrix} hv \\ huv \\ hv^2 + \frac{1}{2}gh^2 \end{bmatrix}, \quad \mathbf{S}(\mathbf{U}) = \begin{bmatrix} 0 \\ gh(s_{ox} - s_{fx}) \\ gh(s_{oy} - s_{fy}) \end{bmatrix}, \quad (2)$$

151 where x and y are the spatial (horizontal) coordinates; t is time; $h(x, y, t)$ is the water
 152 depth; $u(x, y, t)$ and $v(x, y, t)$ denote the x and y components of the depth-averaged flow
 153 velocity, respectively; $s_{ox} = -\partial z/\partial x$ and $s_{oy} = -\partial z/\partial y$ are the bed slopes in the x
 154 and y directions, respectively, and $z(x, y)$ is the terrain elevation (assumed constant in
 155 time); s_{fx} and s_{fy} denote the friction slopes in the x and y directions, respectively. The
 156 friction slopes can be modeled using Manning-Strickler's expression, $s_{fx} = n^2 u \sqrt{u^2 + v^2} h^{-4/3}$,
 157 $s_{fy} = n^2 v \sqrt{u^2 + v^2} h^{-4/3}$, where n is the Manning coefficient. Solutions $\mathbf{U} = (h, hu, hv)^T$
 158 to this system (subject to well-posed boundary and initial conditions) can be computed
 159 by several numerical methods available, as discussed in the Introduction.

In this paper we propose a ML-based solution to this problem, whereby the input layer \mathbf{x} represents the independent variables and parameters of the problem, $\mathbf{x} = (x, y, t, n, z)$, and the trained model \aleph is expected to provide an approximate solution for $h(\mathbf{x})$, $hu(\mathbf{x})$ and $hv(\mathbf{x})$ in the corresponding domain; in other words:

$$\mathbf{U}(\mathbf{x}) \cong \tilde{\mathbf{U}}(\mathbf{x}) = \aleph(\mathbf{x}; \Gamma), \quad (3)$$

160 where $\tilde{\mathbf{U}}(\mathbf{x})$ denotes the output from the PINN, which is in turn defined by the group
 161 of trainable parameters Γ (e.g., convolutional filter, weights and biases). The PINN mod-
 162 els proposed in this paper are trained by minimizing the composite loss function, defined
 163 as:

$$\mathcal{L} = \lambda_1 \cdot \mathcal{L}_p + \lambda_2 \cdot \mathcal{L}_b + \lambda_3 \cdot \mathcal{L}_0, \quad (4)$$

164 where \mathcal{L} (a scalar) is the loss function to be minimized, λ_{1-3} are the vectors of penalty
 165 coefficients for every specific loss term; namely, \mathcal{L}_p penalizes the residuals of the SWEs,
 166 \mathcal{L}_b and \mathcal{L}_0 penalize the BCs (subscript b) and ICs (subscript 0) residuals, respectively.
 167 These loss terms are in turn given by:

$$\mathcal{L}_p = \frac{1}{N} \sum_{i=1}^N |\partial_t \tilde{\mathbf{U}}_i + \partial_x \mathbf{F}(\tilde{\mathbf{U}}_i) + \partial_y \mathbf{G}(\tilde{\mathbf{U}}_i) - \mathbf{S}(\tilde{\mathbf{U}}_i)| \quad (5a)$$

$$\mathcal{L}_b = \frac{1}{N_b} \sum_{i=1}^{N_b} |\tilde{\mathbf{U}}_{b,i} - \mathbf{U}_{b,i}| \quad (5b)$$

$$\mathcal{L}_0 = \frac{1}{N_0} \sum_{i=1}^{N_0} |\tilde{\mathbf{U}}_{0,i} - \mathbf{U}_{0,i}| \quad (5c)$$

168 The tilde symbol ($\tilde{}$) denotes neuronal network output and the subscript $i \in [1, N]$
 169 refers to the i^{th} collocation point. N represents the number of collocation points, which
 170 in this paper is defined from a uniformly discretized domain of the independent variables
 171 $N = n_x \times n_y \times n_t$, where n_x , n_y and n_t are the number of points used to discretize the
 172 domain along the x , y and t coordinates, respectively. The boundaries of the spatio-temporal
 173 domain are represented by a subset of N ; in particular, the model will employ $N_b < N$
 174 and $N_0 < N$ points to define the BCs and ICs, respectively.

175 For each approximate solution produced by the PINN, the partial derivatives in
 176 Eq. 5a are computed through the method of automatic differentiation (autodiff) (Paszke
 177 et al., 2017), which back-propagates derivatives from the outputs to the targeted inputs
 178 through the chain rule to compute the desired derivatives (Cai et al., 2021; Baydin et
 179 al., 2018). Thus, the partial derivatives of the approximate solution with respect to the
 180 independent variables can be computed without the errors common to numerical differ-
 181 entiation techniques. The loss function is minimised using the gradient descent method,
 182 with gradients of the loss function with respect to trainable parameters computed by back-
 183 propagation. These parameters can be updated either using all, or a subset (batch) of
 184 the collocation points.

185 One significant difficulty of solutions to flow problems modeled by the SWEs is the
 186 so-called wet-dry front issue (i.e., moving boundary). Physically, the value of the flow
 187 depth h cannot be negative. Areas of the domain where such solutions may be obtained
 188 correspond to dry areas, which are not governed by the SWEs. To overcome this prob-
 189 lem, we set $\mathcal{L}_p = 0$ if the predicted value of \tilde{h} is negative. This ensures that the model
 190 does not penalize making predictions outside the wet domain.

191 Figure 1 shows a diagram illustrating the overall modeling framework proposed in
 192 this paper for solving the SWEs by a PINN method. Note that the collocation points

193 can be chosen randomly in the space-time domain and their number prescribed. The general
 194 steps are outlined below.

- 195 1. Define the architecture of the PINN
 196 2. Initialize the hyperparameters for the PINN
 197 3. Compute the outputs from the PINN with given inputs
 198 4. Compute the derivatives with respect to x, y, t and the corresponding loss \mathcal{L}
 199 5. Update the PINN based on \mathcal{L}
 200 6. Repeat steps 3 to 5 until the end of the user-prescribed number of training epochs

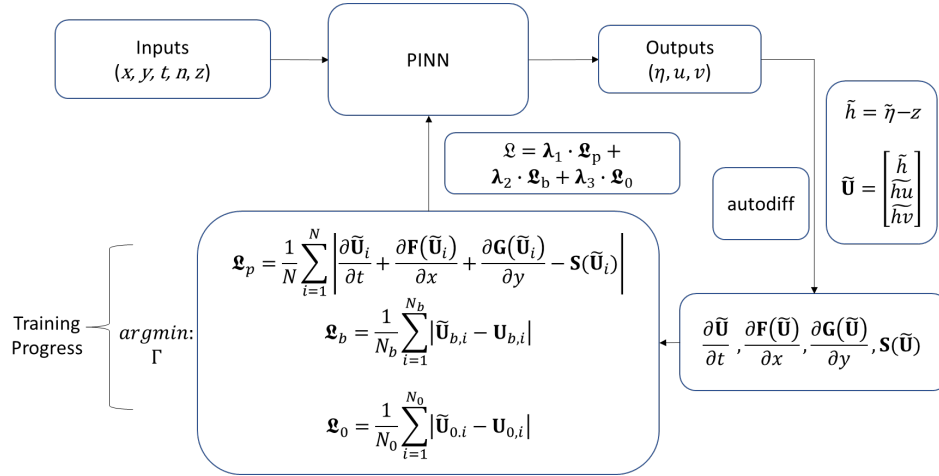


Figure 1. A schematic diagram of a physics informed neuronal network (PINN) for finding approximate solutions to the shallow water equations.

201 2.2 Fully Connected Neural Network

202 The FCNN is the most commonly applied ML model and often includes more than
 203 one hidden layer. Every hidden layer receives the signals from the previous layer, per-
 204 forms basic computations defined at each neuron, and passes the results to the next layer
 205 (Haykin, 2009). Figure 2 shows a diagram of a FCNN. Mathematically, the basic function
 206 of the output for the j^{th} hidden layer \mathbf{y}_j is:

$$\mathbf{y}_j = \varphi(\mathbf{W}_j \mathbf{y}_{j-1} + \mathbf{b}_j) \quad (6)$$

207 where \mathbf{W} is the matrix of weights, \mathbf{b} is the vector of biases and $\varphi(\cdot)$ is the activation func-
 208 tion.

209 In the proposed method, solutions for each output variable $\eta(\mathbf{x}) = h(\mathbf{x}) + z$, $hu(\mathbf{x})$,
 210 $hv(\mathbf{x})$ are approximated by 3 separate FCNNs with the same structure, as illustrated in
 211 Figure 2. Every FCNN receives the same raw inputs. As a result, the trainable param-
 212 eters of the solution for each output variable are decoupled. This can significantly im-
 213 prove the prediction accuracy in multivariate problems, especially when the distributions
 214 and magnitudes of the variables are significantly different (e.g., Sun et al., 2020; Gao et
 215 al., 2021; Guo et al., 2020, and others).

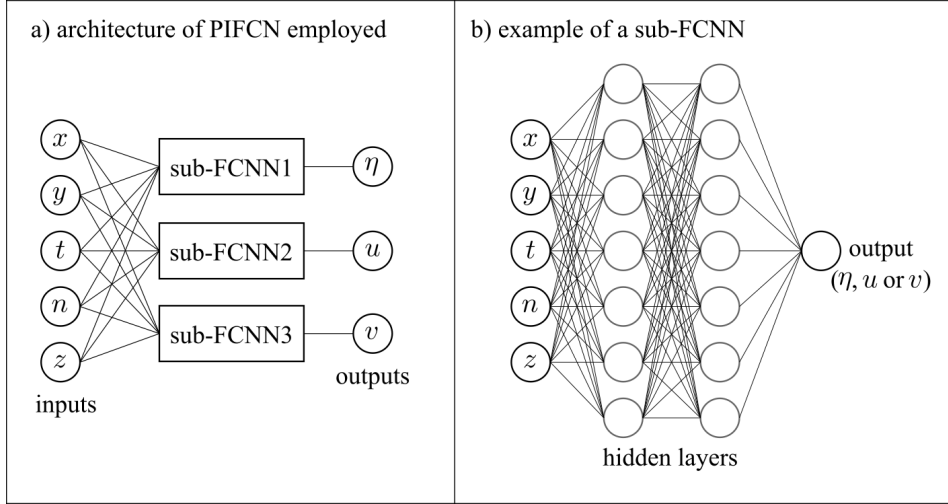


Figure 2. (a) The architecture of the physics-informed fully connected networks (PIFCNs) employed in this paper. (b) An example of a typical fully connected neuronal network (FCNN) which is employed as a sub-network within the PIFCN to predict each individual output; as illustration, 2 hidden layers with 7 neurons each are shown, but these hyperparameters are varied in this study.

216

2.3 Convolutional Neural Network

217

218

219

The CNN adds one or more convolutional layers that extract features of the raw training dataset before feeding this onto the typical hidden layers used to build FCNNs. The general expression for the convolution operator \star with 1 stride is:

$$(\mathbf{s} \star \mathbf{k})_i = \sum_{j=1}^n k_j s_{i+j-1} \quad i = 1, 2, \dots, m - n + 1 \quad (7)$$

220

221

222

223

224

225

where \mathbf{s} denotes the input signal vector of length m (in this paper, this is \mathbf{x}), and \mathbf{k} denotes the trainable filter of length n . The convolution operation is to slide the preset convolutional filter over the signal input and output the signal with a shorter length (i.e., the input vector is shortened by $n - 1$ elements). The shorter length of the convolved output signal allows the following typical hidden layer to have fewer neurons, facilitating the network's learning of large-scale problems with high complexity (Gao et al., 2021).

226

227

228

229

Figure 3 shows the structure of the CNN used in this paper. The trainset is generated from a number of points (i.e., collocation points) randomly sampled from a grid of equally spaced points. Each output variable, $h(\mathbf{x})$, $hu(\mathbf{x})$, $hv(\mathbf{x})$, is also predicted by a separate sub-CNN.

230

2.4 PINN design

231

232

233

234

235

236

237

The accuracy and computational performance of the PINNs described in the previous sections will be assessed and compared against the corresponding performance and solutions by a conventional FV model. There is currently no universal design approach to determine the optimal, or even appropriate, structure for a neural network (Bihlo & Popovych, 2022). The general selection rule for PINN design is to find a structure with the lowest possible complexity that achieves the desired accuracy of prediction. This rule can usually help provide an AI model with quick learning speed and improved predic-

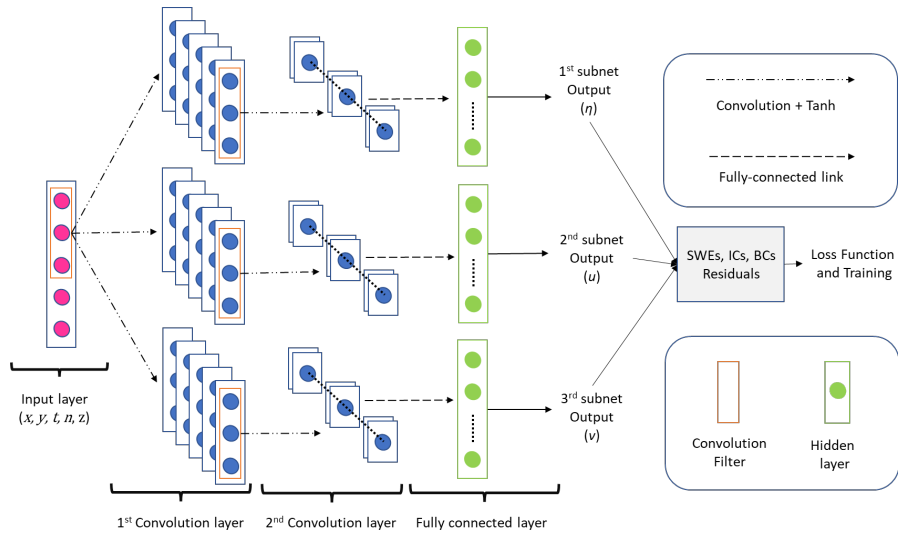


Figure 3. An example of the structure of a CNN-based model with 3 subnets for solving free-surface flow problems. Each output variable (η, u or v) is approximated by a separate CNN with the above structure; all sub-networks receive the same inputs. Each CNN has two convolutional layers and one hidden layer. The hyperparameters shown in the figure are discussed in Section 2.4.

238 tion capabilities while avoiding overfitting issues (Blumer et al., 1987). In this paper, the
 239 final decision for the model structure (i.e. hyperparameters such as the number of neurons,
 240 hidden layers, and convolutional layers and channels in the case of CNN) was made
 241 after many practical attempts (see Appendix A). As the evaluation of the PINNs per-
 242 formance in this paper consists of two, often competing, criteria (accuracy and compu-
 243 tational cost), it may be difficult to find a single assessment metric to guide the PINNs
 244 design. Hence, we give priority to accuracy by gradually increasing the complexity of the
 245 PINNs until similar or higher accuracy than benchmark results (e.g. from an analyti-
 246 cal solution or a finely resolved FV simulation) is attained. Generally, in our design it-
 247 erations, the number of hidden layers and the corresponding neurons for building PINNs
 248 (i.e., PIFCN and PICN) started from 1 and 50, respectively. The number of convolutional
 249 layers and corresponding channels started from 1 and 5, respectively. For both PICN and
 250 PIFCN we use the hyperbolic tangent activation function (Tanh). Note that the PINN
 251 design may change significantly depending on domain and flow conditions; i.e., it can be
 252 very problem-specific. It is also important to recognize that the networks chosen do not
 253 represent the strictly optimal structure, but only the best out of the subset of structures
 254 that were tested.

255 For improving the learning speed and reducing the effect of parameter initializa-
 256 tion, the Batch Normalization method of Ioffe and Szegedy (2015) was used, which nor-
 257 malizes the signals between adjacent convolutional or hidden layers. The Adam optimizer
 258 (Kingma & Ba, 2014), along with the ‘1-cycle’ (Smith & Topin, 2019) strategy was used
 259 to control the training of the PINNs. The PINNs were implemented on the Pytorch plat-
 260 form Paszke et al. (2017). The FV simulation and the training of the PIFCNs and PICNs
 261 were performed using the University of Southampton’s supercomputer Iridis 5 ensuring
 262 that the exact same hardware resources were employed (thus ensuring a fair compari-
 263 son across all simulations performed).

264 3 Case studies

265 This section describes three case studies used to test the PINNs, comparing their
 266 results against analytical and numerical (Finite Volume) solutions. The first and second
 267 tests are idealized 1D (unsteady and steady, respectively) flow problems for which an-
 268 analytical solutions are available. However, simulations were performed on a 2D domain
 269 since the ultimate aim is to employ the PINNs developed here in 2D flow problems. The
 270 third test case is an unsteady two-dimensional simulation of a real-world flood event that
 271 took place in the Tiber river, Italy. This case study has been previously employed to eval-
 272 uate the performance of other numerical models (e.g., Morales-Hernández et al., 2016;
 273 Shamkhalchian & de Almeida, 2021, and others).

274 Topographic data used in all tests are defined by square grids with different res-
 275 olutions. The grid points are used to generate a triangular mesh for the FV model. These
 276 are also employed, along with defined temporal steps, as the collocation points for the
 277 PINNs training. The accuracy of the solutions will be assessed by the root mean square
 278 error, \mathcal{R} , of the outputs of each model relative to the benchmark solution. For example,
 279 in the evaluation of accuracy for the prediction of h with N_p output points, the perfor-
 280 mance metric is defined as $\mathcal{R}_h = \sqrt{\sum (h_i - \tilde{h}_i)^2 / N_p}$, where h_i is the benchmark solu-
 281 tion (i.e., the analytical solution when available, or the solution of the FV model at fine
 282 resolution). The second performance metric we employ is the computational cost, \mathcal{T}_c , which
 283 represents training time for the PINNs (PICN and PIFCN), and run time for the FV model.
 284 In the results presented in the following sections, predictions by the FV, PIFCN and PICN
 285 models are labelled with the different resolutions used. For example, FV (10) represents
 286 a 10 m resolved simulation using the FV hydraulic model, and PICN (50) refers to the
 287 prediction of the PICN trained from a 50 m resolved dataset.

288 3.1 Flood wave propagation over a horizontal plane

289 The first test case is a one-dimensional simulation of an inundation wave propa-
 290 gating over a horizontal bed. A time-dependent BC is imposed at $x = 0$. Under the
 291 idealized assumption of a flow velocity that is constant in space and time, the problem
 292 admits an analytical solution which can be expressed as (Hunter et al., 2005):

$$293 \quad h_a(x, t) = \left\{ \frac{7}{3} (n^2 u^2 (x - ut)) \right\}^{3/7}, \quad (8)$$

294 where the subscript a is used to denote the analytical solution. The domain used is a
 295 100 m wide, 1200 m long channel. The constant velocity is set as $u(x, t) = 0.29 \text{ ms}^{-1}$
 296 and the boundary condition $h(x = 0, t)$ is given by Eq. 8. The domain is initially dry,
 297 i.e., $h(x, t = 0) = 0$. Manning's coefficient n is set to $0.03 \text{ sm}^{-1/3}$. The duration of
 298 the simulation is 3600 s. The FV model was run at resolutions of 1, 2, 5 and 10 m, while
 299 the PINN models were trained with datasets defined at resolutions of 10, 25, 50 and 100
 300 m. While the time step of the explicit FV scheme is controlled by the Courant-Friedrichs-
 301 Lewy (CFL) stability condition, the regression approximation implemented by the PINN
 302 model is not limited by temporal resolution. However, the time step adopted to train
 303 the PINN model is a factor that clearly affects both accuracy and computational per-
 304 formance. For this test, we use a temporal resolution for the PINN of 300 s. The selected
 batch size is set as the full set of collocation points $n_x \times n_y \times n_t$.

305 The architecture of the PICN consists of 2 convolutional layers (the first and sec-
 306 ond layers have 5 and 20 channels, respectively) and 1 fully connected hidden layer with
 307 50 neurons. The architecture for the PIFCN consists of 3 fully connected hidden layers,
 308 each of which has 1000 neurons.

309 Figures 4 and 5 illustrate the values of $h(x, y = 50\text{m})$ and $hu(x, y = 50\text{m})$ (left
 310 vertical axes), and the corresponding error (right vertical axes) $\epsilon_h(x, y = 50\text{m}) = h(x, y =$

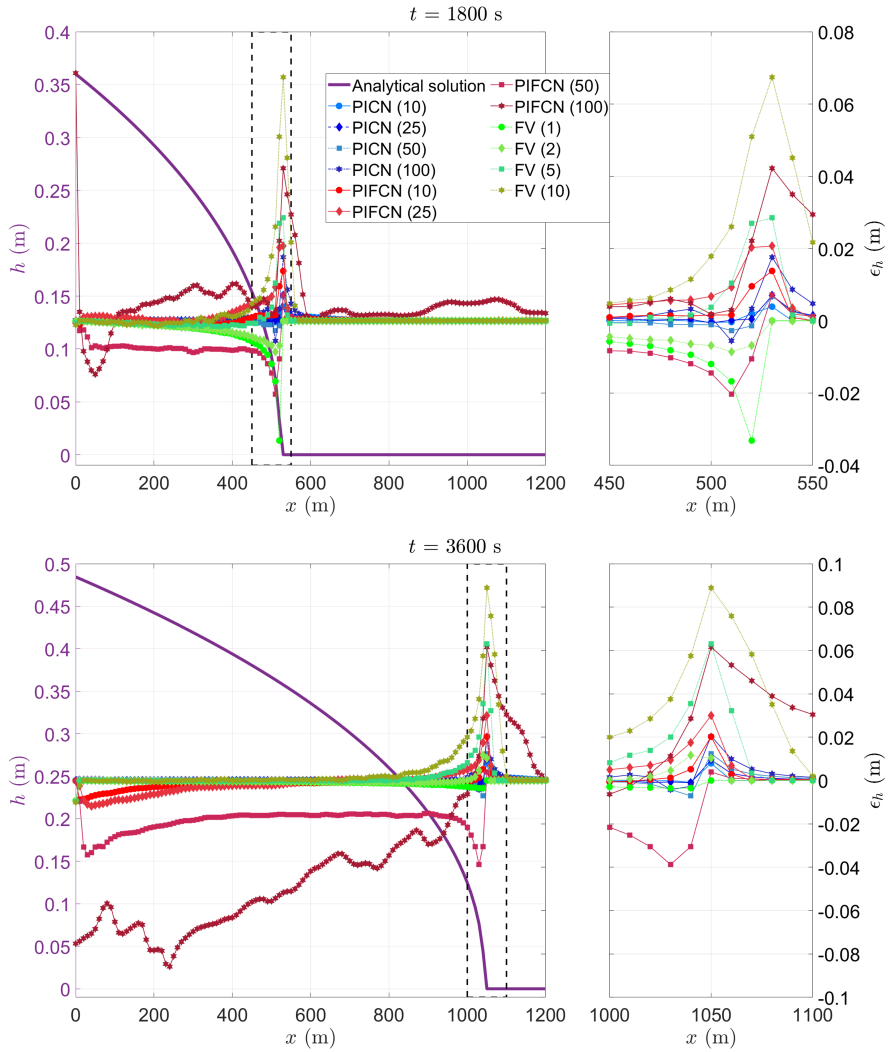


Figure 4. Test 1: Longitudinal profiles ($y = 50 \text{ m}$) of water depth errors ϵ_h relative to the analytical solution obtained by each of the models at $t = 1800 \text{ s}$ (top) and $t = 3600 \text{ s}$ (bottom), shown against right y -axis. The analytical solution for h (purple line) is plotted against the left y -axis; note that the right-side figure is the enlarged version of the rectangular box in the left-side figure; both figures share the same right y -axis.

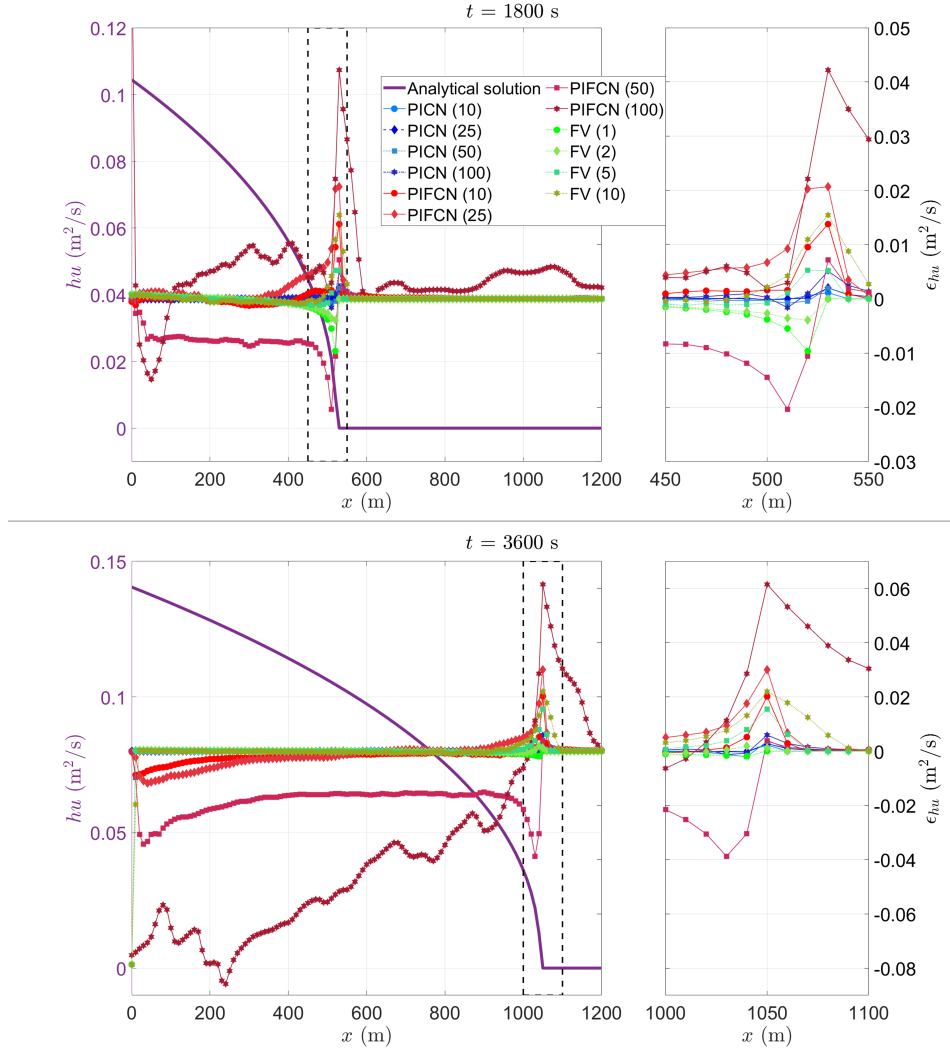


Figure 5. Test 1: Longitudinal profiles ($y = 50$ m) of water depth errors ϵ_{hu} relative to the analytical solution obtained by each of the models at $t = 1800$ s (top) and $t = 3600$ s (bottom). The analytical solution for hu (purple line) is plotted against the left y -axis; note that the right-side figure is the enlarged version of the rectangular box in the left-side figure; both figures share the same right y -axis.

311 $50\text{m}) - h_a(x, y = 50\text{m})$ and $\epsilon_{hu}(x, y = 50\text{m}) = \tilde{h}u(x, y = 50\text{m}) - (hu)_a(x, y = 50\text{m})$
 312 computed by all three models at $t = 1800$ and 3600 s, respectively. Values of hv are not
 313 reported as the test case is fundamentally one-dimensional. Overall, all the water depth
 314 predictions, with the exception of PIFCN (100), show good agreement with the analyt-
 315 ical solution (i.e. most results displaying $|\epsilon| < 0.01\text{m}$). As the position of the wet-dry
 316 front predicted by the models does not exactly match the analytical solution, and the
 317 front is steep at that point, errors are larger in this region. PICN and FV both show sim-
 318 ilar prediction accuracy of both h and hu , whereas PIFCNs with coarsely resolved train-
 319 sets (i.e., 50 m and 100 m) provide higher prediction errors of hu .

320 Figure 6 shows \mathcal{R}_h (relative to the analytical solution h_a) for all results obtained
 321 with the PICN, PIFCN, and FV models as a function of the corresponding computational
 322 time \mathcal{T}_c . The sum to compute \mathcal{R}_h is over all collocation points; i.e., spanning the whole
 323 spatio-temporal domain. In this figure, the various points (blue and red) presented for
 324 each PINN model represent solutions obtained at different epochs during the training
 325 of the networks, which correspond to different computation time and level of accuracy.
 326 The green cross points represent the simulation accuracy and computation time for the
 327 FV model. The results in this figure are based on model (i.e. PICN, PIFCN, and FV)
 328 outputs at the same grid points selected from the entire domain with a spatial and tem-
 329 poral resolution of 10 m and 360 s. Predictions of hu follow the general pattern observed
 330 for h on Figure 6 and are not reported here to avoid repetition. Figure 6 allows us to
 331 comparatively assess the performance of the models tested in terms of their speed-accuracy
 332 trade-off. Based on this criterion, a model performs better than another when it provides
 333 more accurate results under the same computational time, or vice-versa; in other words,
 334 the best results are those closest to the bottom left corner of the plot.

335 Figure 6 shows that FV (10) and FV (5) produce sub-centimetre \mathcal{R}_h (which is usu-
 336 ally considered a good level of accuracy for many applications) at least one order of mag-
 337 nitude faster than the PINN models, whereas FV (2) takes slightly longer than PICNs
 338 (for the same level of accuracy), and FV (1) only outperforms PIFCN (10) in terms of
 339 the speed-accuracy trade-off. All PINNs except PIFCN (100) show the potential to achieve
 340 better accuracy of prediction than the FV model at the highest resolution tested here
 341 (1 m), provided they are trained for long enough. PICNs provide a faster solution (for
 342 similar \mathcal{R}_h values) than PIFCNs. Also, for PIFCN, the trainset size (which in this case
 343 is determined by the resolution) did not significantly affect its maximum accuracy at res-
 344 olutions ≤ 50 m, whereas the accuracy of the FV model continues to improve as the mesh
 345 is refined below 10 m.

346 3.2 Subcritical steady flow over an undulating bed

347 The second test case represents a 1D, steady, non-uniform flow over an undulat-
 348 ing bed, for which an analytical solution is available (see MacDonald, 1996; de Almeida
 349 & Bates, 2013; Delestre et al., 2013). This test case will be used to evaluate the solu-
 350 tion obtained by the PICN and PIFCN in a problem with variable topography. The (rect-
 351 angular) channel is 1000 m long, and Manning’s coefficient n is set to $0.03 \text{ sm}^{-1/3}$. The
 352 constant inflow discharge per unit width of the channel is $q_x = uh = 2 \text{ m}^2\text{s}^{-1}$, and the
 353 downstream water depth is $\frac{9}{8}$ m. We prescribe the following function representing the
 354 water depth $h(x)$ (which is the benchmark solution against which the PINN approxima-
 355 tions will be compared):

$$h(x) = \frac{9}{8} + \frac{1}{4} \sin\left(\frac{\pi x}{500}\right). \quad (9)$$

356 We model this 1D problem in a 2D domain using a width of 50 m (and $q_y = 0$)
 357 for the reasons discussed previously. Also, although the solution sought is for a steady
 358 flow problem, the steady condition was reached via an unsteady flow simulation, as the

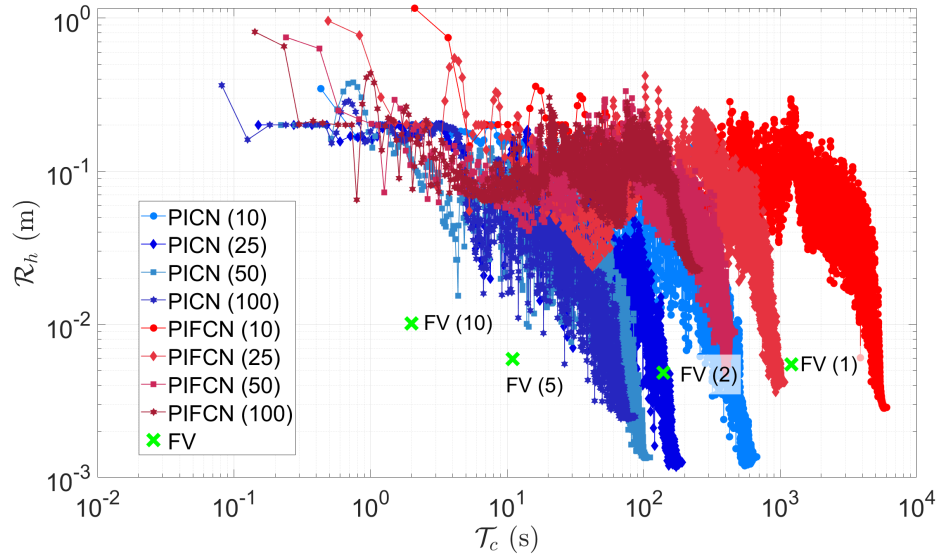


Figure 6. Test 1: Values of \mathcal{R}_h as a function of \mathcal{T}_c (training time for PICN and PIFCN and run time for FV); note that the right-most point of each cloud corresponds to the highest accuracy that any given PINN can achieve. The number in brackets represents the resolution (in meters) of the training data set (for PICN and PIFCN) or mesh (for the FV model).

359 object of this paper is to test approximate methods to solve the time-dependent SWEs.
 360 The unsteady simulations were run from an initially dry domain over a period of 20 hours,
 361 whereby the upstream BCs increase linearly with time from zero to the aforementioned
 362 constant values over the first 10 hours of the simulation.

363 The training dataset for PICN and PIFCN was obtained from grids resolved at 5,
 364 10, 25 and 50 m at the following times: 0, 1, 3, 5, 10, 15 and 20 hours. The selected batch
 365 size is $2/7 \times N$, where the value $2/7$ comes from trial and error (larger batch sizes de-
 366 creased the accuracy of the results). The FV model was run at resolutions of 2, 5 and
 367 10 m.

368 For this case, the architecture of the PICN consists of 2 convolutional layers (the
 369 first and second layers have 5 and 20 channels, respectively) and 1 fully connected hid-
 370 den layer with 50 neurons (same as in Test 1). The architecture of the PIFCN consists
 371 of 3 fully connected hidden layers, each of which has 1000 neurons (different from Test
 372 1).

373 Figure 7 shows the analytical curve for depth profile at the centre of the channel
 374 $h(x, y = 30 \text{ m})$ (left axis) and the corresponding errors of each of the approximate so-
 375 lutions ϵ_h (right axis) predicted by the PICN (blue points), PIFCN (red points), and FV
 376 models (green points). Figure 8 presents similar results but for the variable hu . As the
 377 analytical solution is for the steady state, only the results at the end of the simulations
 378 are assessed. Overall, all models tested delivered results at sub-centimeter level of ac-
 379 curacy for h . The three PICNs showed the lowest errors of both h and hu , followed by
 380 FV (2). Values of ϵ_{hu} obtained from FV models display small (mostly within 1% of the
 381 actual value of hu) spatial variations, while they nearly are constant for both PIFCN and
 382 PICN.

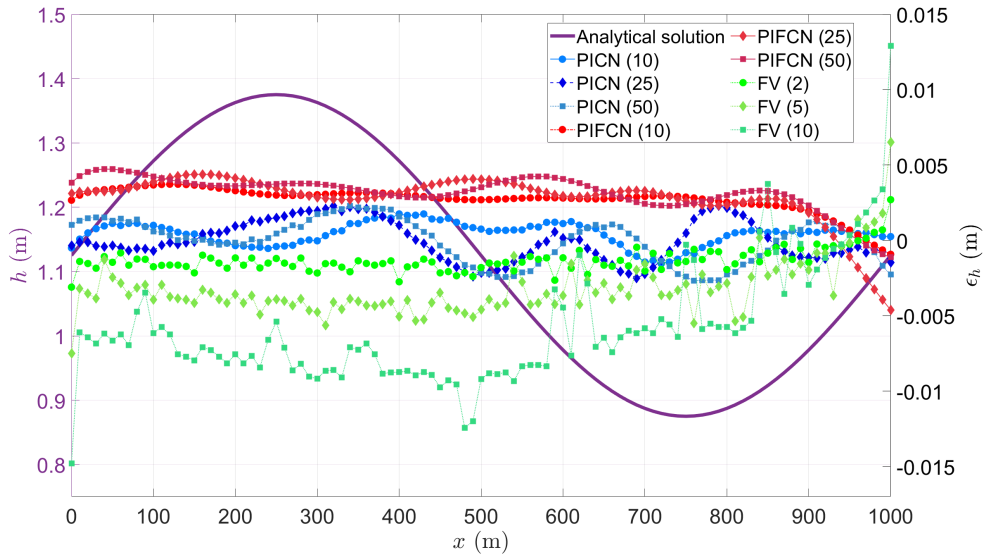


Figure 7. Test 2: Longitudinal profiles ($y = 30$ m) of water depth errors obtained by each of the models at the end of the simulation/training (right y -axis). The analytical solution h (purple line) is plotted against the left y -axis.

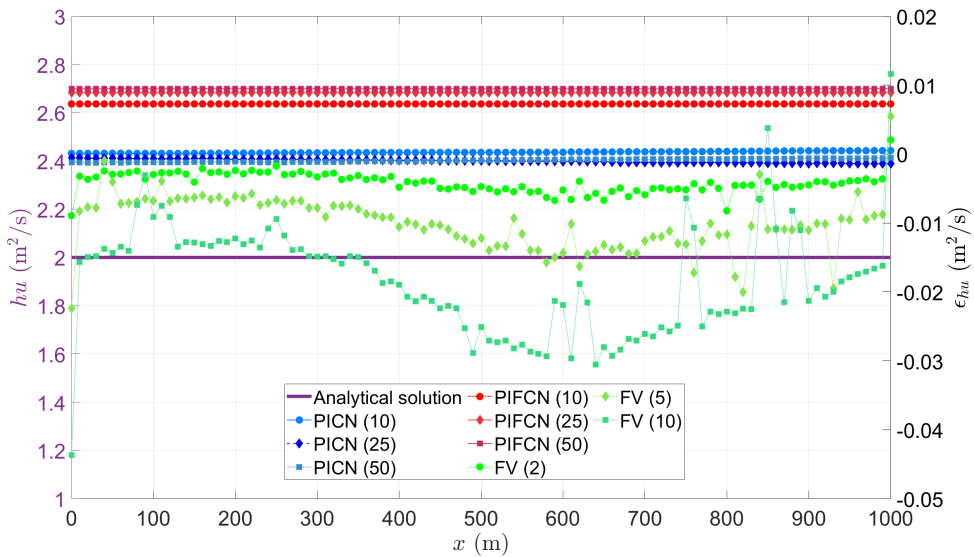


Figure 8. Test 2: Longitudinal profiles ($y = 30$ m) of water depth errors obtained by each of the models at the end of the simulation/training (right y -axis). The analytical solution hu (purple line) is plotted against the left y -axis.

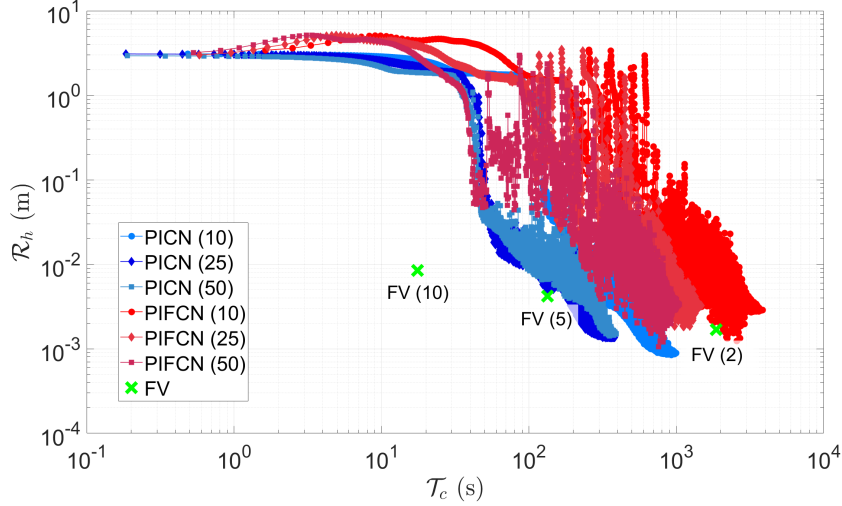


Figure 9. Test 2: Values of \mathcal{R}_h as a function of \mathcal{T}_c (training time for PICN and PIFCN and run time for FV); note that the right-most point of each cloud corresponds to the highest accuracy that any given PINN can achieve. The number in brackets represents the resolution (in meters) of the training data set (for PICN and PIFCN) or mesh (for the FV model).

383 Figure 9 presents the values of \mathcal{R}_h against the corresponding computational time
 384 taken to train the PICN (blue points), PIFCN (red points), and to run the FV model
 385 (green cross points) at different resolutions. The value of \mathcal{R}_h of each model is calculated
 386 from its steady-state predictions of h ; namely: $\mathcal{R}_h = \left(\sqrt{\sum (h_i - \tilde{h}_i)^2 / N_p} \right) \Big|_{t=t_s}$, where
 387 t_s is the time after which a steady state is reached for each PINN or FV model. For the
 388 computation time of FV models described in Figure 9, the value of \mathcal{T}_c is the time required
 389 for all FV models to reach steady state. The results for hu show a pattern similar to that
 390 in Figure 9 and are not presented for conciseness. All simulations achieve sub-centimetric
 391 \mathcal{R}_h , with FV (10) delivering the results at least one order of magnitude faster than the
 392 other solutions. PIFCN (10) was the slowest of all models. Figure 9 shows that the pre-
 393 diction of h from PICN (10) displays the highest accuracy, with an \mathcal{R}_h of 0.85 mm, al-
 394 though this was obtained at a computation time that was 56 times longer than FV (10).
 395 All the PINN results also attain an accuracy higher than or similar to that of FV(2). In
 396 this test case, the relative differences in the prediction accuracy among the PICN mod-
 397 els is less than the difference observed from FV (5) to FV (10). In terms of the influence
 398 of resolution on the computational speed, the PICN is also less sensitive than PIFCN
 399 in this problem.

400 3.3 Simulation of real-world river flooding

401 While Tests 1 and 2 have assessed the ability of PINN models to deal with impor-
 402 tant aspects of flow problems, such as unsteadiness and variable topography, both case
 403 studies represented idealized, one-dimensional problems. In order to investigate the per-
 404 formance of PINNs under more complex and realistic problems, this section presents the
 405 results of simulations of a real-world scenario. The scenario in question is a flood event
 406 that occurred between 27 November and 1 December 2005 in the Tiber river (Morales-
 407 Hernández et al., 2016), which flows from the Apennine Mountains to the Tyrrhenian
 408 Sea in Italy. The reach of river employed in this simulation is approximately 6 km long
 409 and is located near the city of Rome. In this region, the mean discharge of the Tiber river

410 is $267 \text{ m}^3\text{s}^{-1}$, while its peak discharge for a 200-year return period is around $3200 \text{ m}^3\text{s}^{-1}$.
 411 The event modeled in this paper was also previously simulated in Morales-Hernández
 412 et al. (2016) and Shamkhalchian and de Almeida (2021). The domain comprises an area
 413 of $6 \text{ km} \times 2 \text{ km}$. The duration of the event simulated is 113 hours. The values of Man-
 414 ning’s coefficient n used are the same as in Morales-Hernández et al. (2016) and Shamkhalchian
 415 and de Almeida (2021); namely, $n = 0.035 \text{ sm}^{-1/3}$ for the main channel, and $n = 0.0446$
 416 $\text{sm}^{-1/3}$ for the floodplains.

417 The boundary conditions were obtained from Morales-Hernández et al. (2016), and
 418 correspond to the time series of flow discharge and water surface elevation at the upstream
 419 and downstream sections of the river at the boundary of the computational domain. The
 420 initial conditions $\mathbf{U}(x, y, t = 0)$ were defined from the results of the FV model under
 421 steady-state conditions ($Q = 374 \text{ m}^3\text{s}^{-1}$) performed at 5 m resolution. PINNs were trained
 422 from datasets resolved at 50, 100 and 200 m, while the FV model was run using meshes
 423 generated from gridded data at resolutions of 10, 25 and 50 m. The corresponding tempo-
 424 ral resolution for the trainset for the PINNs is 4 hours. The batch size was set to one
 425 third of the total number of collocation points.

426 For this test case, the architecture of the PICN consists of 2 convolutional layers
 427 (the first and second layers have 10 and 40 channels, respectively) and 1 fully connected
 428 hidden layer with 100 neurons. The architecture of the PIFCN consists of 3 fully con-
 429 nected hidden layers, each having 2000 neurons. Our tests showed that further increas-
 430 ing the network complexity would not improve the model’s prediction accuracy, and may
 431 substantially increase the training time and/or cause the program to exceed the mem-
 432 ory capacity of the computer resources used.

433 Since an analytical solution is not available for this problem, the results of the FV
 434 simulation at fine resolution (5 m) were used as the benchmark. The accuracy of the so-
 435 lutions of the time-dependent variables is assessed at two cross-sections (located approx-
 436 imately at distances of $1/3$ and $2/3$ of the length of the river within the domain from
 437 the upstream boundary, and hereafter referred to as S1 and S2, respectively) at 1 hour
 438 temporal resolution.

439 Figures 10 and 11 illustrate the time series of prediction errors (right vertical axes),
 440 along with the actual predicted values of the flow depth h and flow discharge Q (left ver-
 441 tical axes) at cross-sections S1 and S2 for each PICN, PIFCN, and FV models. Figure 10
 442 shows that the FV and PIFCN simulations consistently predict larger and lower depths
 443 than the benchmark solution, respectively, at both cross sections in the main channel,
 444 while PICN results display both positive and negative values of ϵ_h . Results from PICNs
 445 at S1 and S2 are markedly more accurate than those delivered by PIFCNs and the coarse-
 446 resolution FV models. For example, FV (50) and FV (25) produced results that devi-
 447 ate substantially (i.e. up to approximately 1.2 m and 2.5 m at S1 and S2, respectively)
 448 from the benchmark solution. On the other hand, FV (10) generally produced the most
 449 accurate depth predictions out of all models tested. The ability of the models to predict
 450 flow velocities (and therefore, the volumetric flow rate Q) is assessed by $\epsilon_Q = \tilde{Q} - |Q|$,
 451 where $Q = \int h \mathbf{U} \cdot \mathbf{n} dl$ is the total discharge; l is the length along the cross-sections (i.e.,
 452 S1 and S2, which span across the whole domain) and \mathbf{n} is the unit vector normal to the
 453 cross-section. Figure 11 shows the predicted errors ϵ_Q obtained by all models as a func-
 454 tion of time. These results are markedly different from those previously presented for
 455 ϵ_h . Namely, all FV models display values of ϵ_Q that are substantially smaller than those
 456 predicted by PICN and PIFCN models. The maximum values of ϵ_Q for PICN and PIFCN
 457 are more than 50% and 70% of the benchmark (FV (5)) in S2, respectively. The pos-
 458 sible reason behind these results might be that the water surface ($\eta = h + z$) presents
 459 much less spatial variation than Q in the domain. However, this hypothesis would need
 460 to be tested thoroughly in the future through a set of specifically designed case studies.

Figure 12 assesses the overall accuracy of temporal prediction for h of each model against the corresponding computational time, using the root-mean-square error metric $\mathcal{R}_h^t = \left(\sqrt{\sum_{(x,y) \in \mathcal{S}} (h_i - \tilde{h}_i)^2 / N_p^t} \right)$, where \mathcal{S} denotes the corresponding cross-section and N_p^t is the number of collocation points in the testset. The best values of \mathcal{R}_h^t (i.e., across all epochs) obtained from all PICN models are within the range of $0.22 \text{ m} < \mathcal{R}_h^t < 0.30 \text{ m}$ (S1) and $0.26 \text{ m} < \mathcal{R}_h^t < 0.34 \text{ m}$ (S2), while FV (10) delivered $\mathcal{R}_h^t = 0.29 \text{ m}$ (S1) and 0.35 m (S2), and results from FV (25) and FV (50) were substantially less accurate. It is interesting to note that PINN models trained with coarse datasets (e.g., 200 m) do not necessarily deliver poorer accuracy compared to their fine resolution counterparts; this contrasts with what is typically observed in simulations with traditional numerical methods such as FV. Figure 12 also indicates that PICN models may offer improved depth predictions at lower cost than a FV model. For example, the accuracy of depth predictions by PICN (200) is better than the accuracy delivered by FV (10), while the computational cost is more than one order of magnitude lower. Overall, the PICN shows better h prediction performance than PIFCN and FV in terms of the speed-accuracy trade-off.

Figure 13 shows examples of flood depth maps at $t = 32$ hours obtained by the FV model at resolutions of 5 m and 25 m, along with those produced by PICN and PIFCN at 100 m resolved trainsets. As expected from the results presented in Figure 10, FV (25) overestimates h during the peak time (which also translates into a larger flooded area), while the opposite is observed for PICN (100) and PIFCN (100). Further spatial analysis can be seen in Appendix B.

4 Concluding remarks

In this paper, two physics-informed neuronal networks (PINNs) were developed to predict the evolution of free-surface flows typically modeled by the shallow water equations (SWEs). The PINN formulation eliminates the need for labeled data, which is typically required in supervised learning. This is achieved by defining a loss function that combines the SWEs, the boundary conditions (BCs) and initial conditions (ICs), allowing the trained PINN to serve as an alternative method for solving the SWEs. The two PINNs developed and tested here vary in their architecture and main features. The first is based on the fully-connected neural network (PIFCN), and the second on the convolutional neural network (PICN) approach.

Three test cases were used to assess the accuracy and computational performance of each model, including two idealized flow problems for which analytical solutions are available, and one simulation of a real-world flood event over a relatively large-scale and complex topography domain. In the idealized problems, the PICN and PIFCN predictions achieved higher accuracy (lower \mathcal{R}_h) than the Finite Volume (FV) solver employed for comparison. However, in these problems, PINNs generally took longer to reach the same prediction accuracy as the coarsely resolved FV model. For the real-world flooding problem, in general, PINNs were able to yield similarly accurate predictions of flow depths compared to finely resolved FV simulations. However, all FV models show much higher accuracy in their predictions of Q . For the spatial analysis of flow depths at the peak of the flood event, PINNs were able to produce flood maps with accuracy (relative to the benchmark finely resolved FV simulation) that is comparable to the results of FV models run at intermediate resolution (e.g., 25 m). Some of the PINN models (e.g., PICN at 100 and 200 m resolution) achieved the same level of accuracy as the 25 m resolution FV model at least one order of magnitude faster. In addition, the prediction capability of PINNs may be less affected by changes in grid resolution than the FV solver, which may represent important advantages in real-world applications where finely resolved topographic data may not always be available. At the same resolution (e.g., 10 m in Tests 1 and 2, or 50 m in Test 3), the training process of PICNs and PIFCNs with random ini-

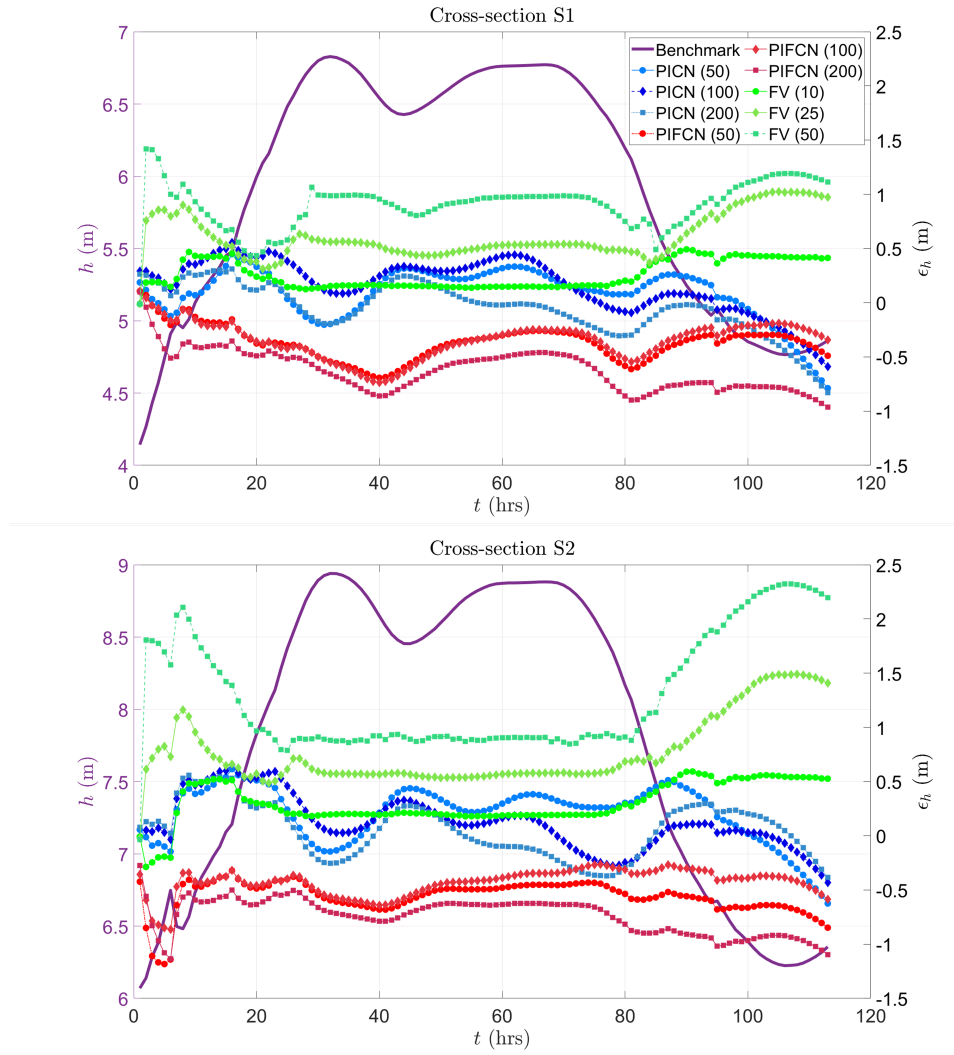


Figure 10. Test 3: Predicted water depths error ϵ_h (plotted against right y -axis) at cross-sections S1 (top) and S2 (bottom) of the main channel in the Tiber river. Benchmark solution (from a finely resolved FV simulation) shown by the purple line against the left y -axis.

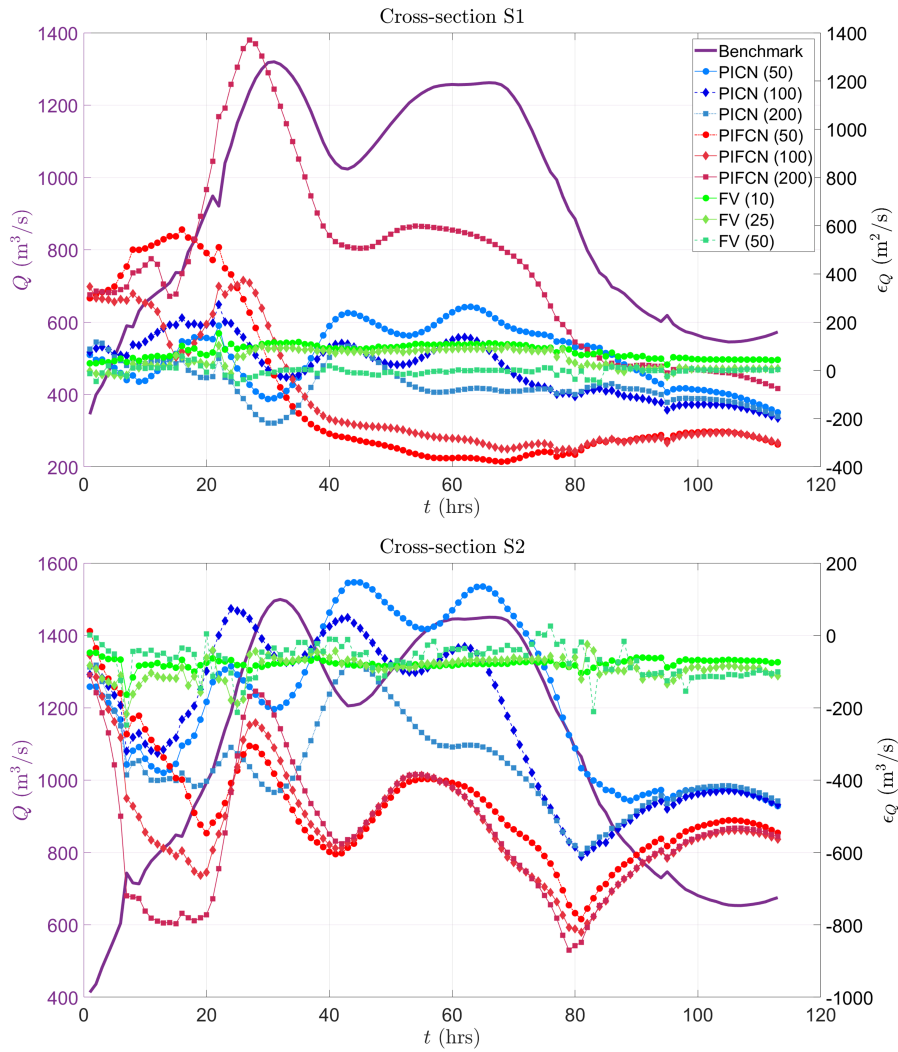


Figure 11. Test 3: Predicted water discharge error ϵ_Q (plotted against right y -axis) at cross-sections S1 (top) and S2 (bottom), which span across the whole domain. Benchmark solution (from a finely resolved FV simulation) shown by the purple line against the left y -axis.

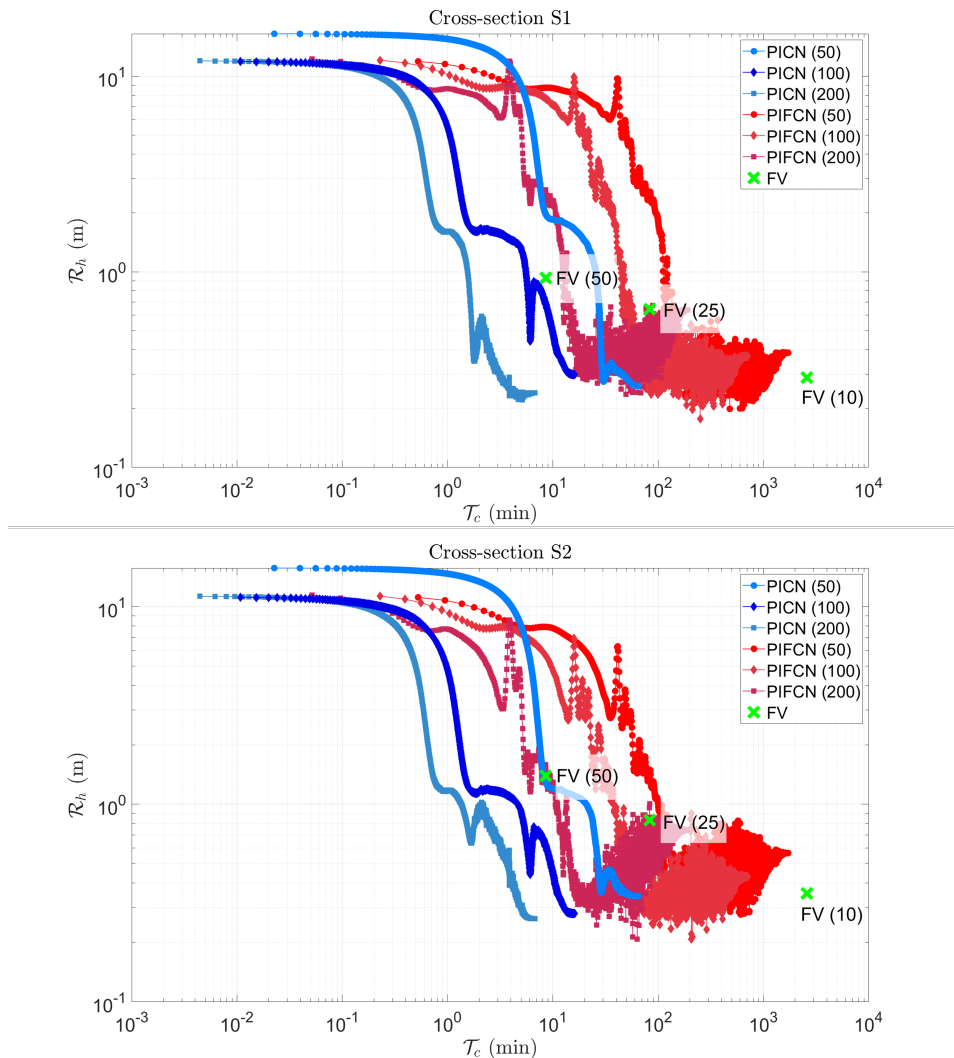


Figure 12. Test 3: \mathcal{R}_h^t as a function of \mathcal{T}_c (training time for PICN and PIFCN and run time for FV) at cross-sections S1 (top) and S2 (bottom) of the Tiber river; note that the right-most point of each cloud corresponds to the highest accuracy that any given PINN can achieve. The number in brackets represents the resolution (in meters) of the training data set (for PICN and PIFCN) or mesh (for the FV model). The benchmark results are those from the FV (5) simulation.

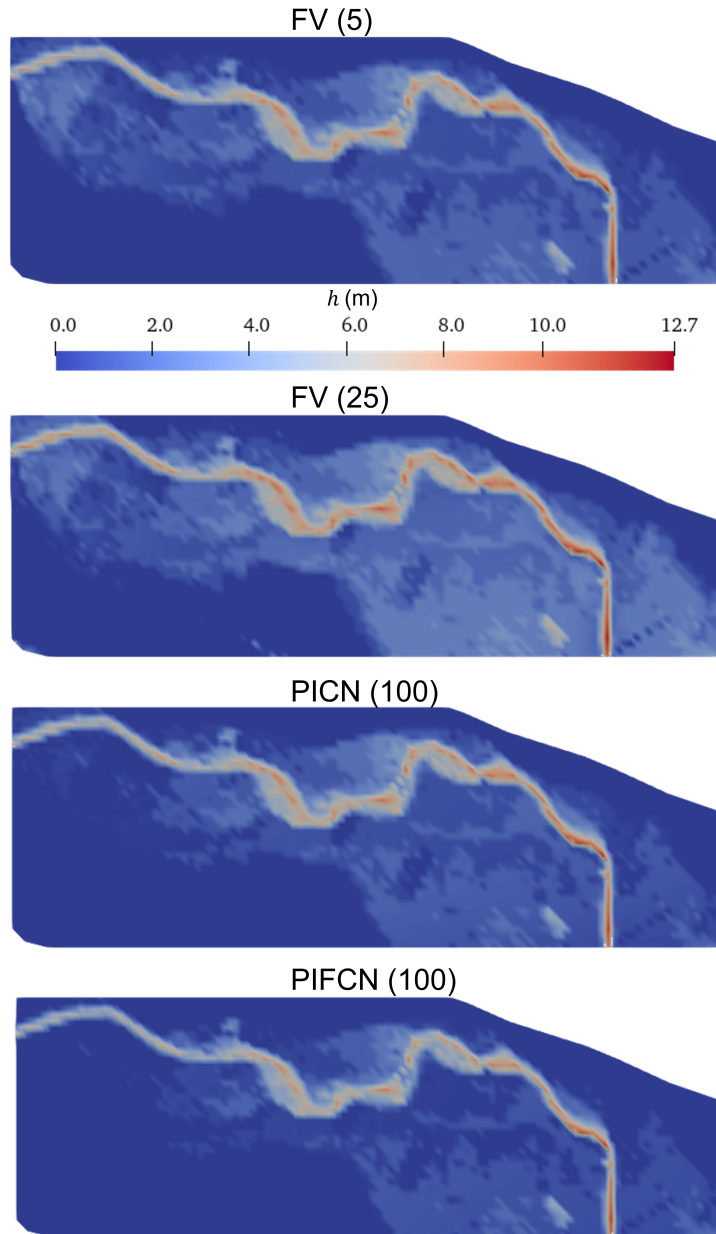


Figure 13. Examples of flood maps at time $t = 32$ hours produced by the FV model and PINNs. Note that FV (5) represents the benchmark results.

512 tialization of weights and biases takes longer than the run time of the FV model. Re-
 513 sults show that, in most circumstances, PICNs usually exhibit better performance in terms
 514 of speed-accuracy trade-off than PIFCNs. However, more comparative tests between PICN
 515 and PIFCN are necessary before reaching general conclusions in this regard.

516 While the results in this paper may not suggest that PINNs can replace other well-
 517 established numerical techniques, they indicate that PINNs (and in particular PICNs)
 518 should be considered as an emerging technique that has the potential to deliver accu-
 519 rate and efficient solutions, and which should be further developed and assessed. Our
 520 results show that the approach might be particularly useful under certain circumstances
 521 which are challenging to conventional techniques. For example, in simulations performed
 522 at coarse resolutions (a typical case in real-world problems), PINN models may achieve
 523 a higher prediction accuracy with a lower computational cost than a FV solver. Since
 524 these techniques are still in their infancy, further research and development may enable
 525 PINNs to become a competitive alternative to simulate flow problems governed by the
 526 SWEs in the near future.

527 5 Open Research

528 The simulation data used for all three test cases in the study are available at the
 529 database from University of Southampton via <https://doi.org/10.5258/SOTON/D2645>
 530 with CC-BY license (Xin Qi, 2023).

531 Acknowledgments

532 The authors acknowledge the use of the IRIDIS High Performance Computing Facility,
 533 and associated support services at the University of Southampton, in the completion of
 534 this work.

535 References

- 536 Alcrudo, F., & Garcia-Navarro, P. (1993). A high-resolution godunov-type scheme
 537 in finite volumes for the 2d shallow-water equations. *International Journal for*
 538 *Numerical Methods in Fluids*, 16(6), 489–505.
- 539 Bale, D. S., Leveque, R. J., Mitran, S., & Rossmanith, J. A. (2003). A wave prop-
 540 agation method for conservation laws and balance laws with spatially varying
 541 flux functions. *SIAM Journal on Scientific Computing*, 24(3), 955–978.
- 542 Baydin, A. G., Pearlmutter, B. A., Radul, A. A., & Siskind, J. M. (2018). Au-
 543 tomatic differentiation in machine learning: a survey. *Journal of Machine*
 544 *Learning Research*, 18, 1–43.
- 545 Bermúdez, M., Cea, L., & Puertas, J. (2019). A rapid flood inundation model for
 546 hazard mapping based on least squares support vector machine regression.
 547 *Journal of Flood Risk Management*, 12(August 2018), 1–14. (Times cited: 6
 548 Flooding papers) doi: 10.1111/jfr3.12522
- 549 Bernard, P.-E., Remacle, J.-F., Comblen, R., Legat, V., & Hillewaert, K. (2009).
 550 High-order discontinuous galerkin schemes on general 2d manifolds applied
 551 to the shallow water equations. *Journal of Computational Physics*, 228(17),
 552 6514–6535.
- 553 Bihlo, A., & Popovych, R. O. (2022). Physics-informed neural networks for the
 554 shallow-water equations on the sphere. *Journal of Computational Physics*, 456,
 555 111024. doi: <https://doi.org/10.1016/j.jcp.2022.111024>
- 556 Blumer, A., Ehrenfeucht, A., Haussler, D., & Warmuth, M. K. (1987). Occam’s raz-
 557 or. *Information Processing Letters*, 24(6), 377–380. doi: [https://doi.org/10](https://doi.org/10.1016/0020-0190(87)90114-1)
 558 [.1016/0020-0190\(87\)90114-1](https://doi.org/10.1016/0020-0190(87)90114-1)
- 559 Botta, N., Klein, R., Langenberg, S., & Lützenkirchen, S. (2004). Well balanced

- 560 finite volume methods for nearly hydrostatic flows. *Journal of Computational*
561 *Physics*, 196(2), 539–565.
- 562 Cai, S., Wang, Z., Wang, S., Perdikaris, P., & Karniadakis, G. E. (2021). Physics-
563 informed neural networks for heat transfer problems. *Journal of Heat Transfer*,
564 143(6).
- 565 Carbonneau, R., Laframboise, K., & Vahidov, R. (2008). Application of machine
566 learning techniques for supply chain demand forecasting. *European Journal of*
567 *Operational Research*, 184(3), 1140–1154.
- 568 Casulli, V. (1990). Semi-implicit finite difference methods for the two-dimensional
569 shallow water equations. *Journal of Computational Physics*, 86(1), 56–74.
- 570 Dawson, C., Westerink, J. J., Feyen, J. C., & Pothina, D. (2006). Continuous,
571 discontinuous and coupled discontinuous–continuous galerkin finite element
572 methods for the shallow water equations. *International Journal for Numerical*
573 *Methods in Fluids*, 52(1), 63–88.
- 574 de Almeida, G. A., & Bates, P. (2013). Applicability of the local inertial approxi-
575 mation of the shallow water equations to flood modeling. *Water Resources Re-*
576 *search*, 49(8), 4833–4844.
- 577 de Almeida, G. A., Bates, P., & Ozdemir, H. (2016). Modelling urban floods at sub-
578 metre resolution: challenges or opportunities for flood risk management? *Jour-*
579 *nal of Flood Risk Management*, 11, S855–S865.
- 580 Delestre, O., Lucas, C., Ksinant, P.-A., Darboux, F., Laguerre, C., Vo, T.-N.-T.,
581 ... Cordier, S. (2013). SWASHES: a compilation of shallow water analytic
582 solutions for hydraulic and environmental studies. *International Journal for*
583 *Numerical Methods in Fluids*, 72(3), 269–300. doi: 10.1002/fld.3741
- 584 El Naqa, I., Li, R., & Murphy, M. J. (2015). *Machine learning in radiation oncology:*
585 *theory and applications*. Springer.
- 586 Ferrari, A., & Vacondio, R. (2022). An augmented hlem ader numerical model par-
587 allel on gpu for the porous shallow water equations. *Computers & Fluids*, 238,
588 105360.
- 589 Gao, H., Sun, L., & Wang, J.-X. (2021). Phygeonet: Physics-informed geometry-
590 adaptive convolutional neural networks for solving parameterized steady-state
591 pdes on irregular domain. *Journal of Computational Physics*, 428, 110079.
- 592 Guo, L., Ye, S., Han, J., Zheng, H., Gao, H., Chen, D. Z., ... Wang, C. (2020). Ssr-
593 vfd: Spatial super-resolution for vector field data analysis and visualization. In
594 2020 *ieee pacific visualization symposium (pacificvis)* (p. 71-80). doi: 10.1109/
595 PacificVis48177.2020.8737
- 596 Haghghat, E., Raissi, M., Moure, A., Gomez, H., & Juanes, R. (2020). A deep
597 learning framework for solution and discovery in solid mechanics. *arXiv*
598 *preprint arXiv:2003.02751*.
- 599 Hanert, E., Le Roux, D. Y., Legat, V., & Deleersnijder, E. (2005). An efficient eu-
600 lerian finite element method for the shallow water equations. *Ocean Modelling*,
601 10(1-2), 115–136.
- 602 Haykin, S. (2009). *Neural networks and learning machines* (Third Edit ed.). Upper
603 Saddle River: Prentice-Hall.
- 604 Henrique, B. M., Sobreiro, V. A., & Kimura, H. (2019). Literature review: Machine
605 learning techniques applied to financial market prediction. *Expert Systems with*
606 *Applications*, 124, 226–251.
- 607 Hornik, K., Stinchcombe, M., & White, H. (1989). Multilayer feedforward networks
608 are universal approximators. *Neural networks*, 2(5), 359–366.
- 609 Hunter, N. M., Horritt, M. S., Bates, P. D., Wilson, M. D., & Werner, M. G. (2005).
610 An adaptive time step solution for raster-based storage cell modelling of flood-
611 plain inundation. *Advances in water resources*, 28(9), 975–991.
- 612 Ioffe, S., & Szegedy, C. (2015). Batch normalization: Accelerating deep network
613 training by reducing internal covariate shift. *CoRR*, abs/1502.03167.
- 614 Jin, X., Cai, S., Li, H., & Karniadakis, G. E. (2021). Nsfnets (navier-stokes flow

- 615 nets): Physics-informed neural networks for the incompressible navier-stokes
 616 equations. *Journal of Computational Physics*, *426*, 109951.
- 617 Juez, C., Murillo, J., & García-Navarro, P. (2014). A 2d weakly-coupled and efficient
 618 numerical model for transient shallow flow and movable bed. *Advances in Wa-*
 619 *ter Resources*, *71*, 93–109.
- 620 Kabir, S., Patidar, S., Xia, X., Liang, Q., Neal, J., & Pender, G. (2020). A deep
 621 convolutional neural network model for rapid prediction of fluvial flood inunda-
 622 tion. *Journal of Hydrology*, *590*, 125481.
- 623 Khan, S., & Yairi, T. (2018). A review on the application of deep learning in system
 624 health management. *Mechanical Systems and Signal Processing*, *107*, 241–265.
- 625 Kingma, D. P., & Ba, J. (2014). Adam: A method for stochastic optimization. *arXiv*
 626 *preprint arXiv:1412.6980*.
- 627 Krishnapriyan, A., Gholami, A., Zhe, S., Kirby, R., & Mahoney, M. W. (2021).
 628 Characterizing possible failure modes in physics-informed neural networks.
 629 *Advances in Neural Information Processing Systems*, *34*.
- 630 Kurganov, A., & Levy, D. (2002). Central-upwind schemes for the saint-venant
 631 system. *ESAIM: Mathematical Modelling and Numerical Analysis*, *36*(3), 397–
 632 425.
- 633 Leandro, J., Chen, A., & Schumann, A. (2014). A 2d parallel diffusive wave model
 634 for floodplain inundation with variable time step (p-dwave). *Journal of Hydrol-*
 635 *ogy*, *517*, 250–259.
- 636 Leskens, J., Brugnach, M., Hoekstra, A. Y., & Schuurmans, W. (2014). Why are
 637 decisions in flood disaster management so poorly supported by information
 638 from flood models? *Environmental modelling & software*, *53*, 53–61.
- 639 LeVeque, R. J., George, D. L., & Berger, M. J. (2011). Tsunami modelling with
 640 adaptively refined finite volume methods. *Acta Numerica*, *20*, 211–289.
- 641 Li, C., Han, Z., Li, Y., Li, M., Wang, W., Dou, J., ... Chen, G. (2023). Physical
 642 information-fused deep learning model ensembled with a subregion-specific
 643 sampling method for predicting flood dynamics. *Journal of Hydrology*, *620*,
 644 129465. Retrieved from <https://www.sciencedirect.com/science/article/pii/S0022169423004079> doi: <https://doi.org/10.1016/j.jhydrol.2023.129465>
- 645 Li, J., Cao, Z., & Borthwick, A. G. (2022). Quantifying multiple uncertainties
 646 in modelling shallow water-sediment flows: A stochastic galerkin frame-
 647 work with haar wavelet expansion and an operator-splitting approach. *Ap-*
 648 *plied Mathematical Modelling*, *106*, 259-275. Retrieved from [https://](https://www.sciencedirect.com/science/article/pii/S0307904X22000579)
 649 www.sciencedirect.com/science/article/pii/S0307904X22000579 doi:
 650 <https://doi.org/10.1016/j.apm.2022.01.032>
- 651 Li, R., Lee, E., & Luo, T. (2021). Physics-informed neural networks for solving mul-
 652 tiscala mode-resolved phonon boltzmann transport equation. *Materials Today*
 653 *Physics*, *19*, 100429.
- 654 Liang, Q. (2011). A structured but non-uniform cartesian grid-based model for the
 655 shallow water equations. *International Journal for Numerical Methods in Flu-*
 656 *ids*, *66*(5), 537–554.
- 657 Liang, Q., & Marche, F. (2009). Numerical resolution of well-balanced shallow wa-
 658 ter equations with complex source terms. *Advances in water resources*, *32*(6),
 659 873–884.
- 660 Liu, Y., & Pender, G. (2015). A flood inundation modelling using v-support vector
 661 machine regression model. *Engineering Applications of Artificial Intelligence*,
 662 *46*, 223–231. (Times cited: 4 Flooding papers) doi: 10.1016/j.engappai.2015.09
 663 .014
- 664 Lynch, D. R., & Gray, W. G. (1979). A wave equation model for finite element tidal
 665 computations. *Computers & fluids*, *7*(3), 207–228.
- 666 MacDonald, I. (1996). *Analysis and computation of steady open channel flow* (Un-
 667 published doctoral dissertation). Citeseer.
- 668 Mahesh, R. B., Leandro, J., & Lin, Q. (2022). Physics informed neural network for
 669

- 670 spatial-temporal flood forecasting. In *Climate change and water security* (pp.
671 77–91). Springer.
- 672 Mao, Z., Jagtap, A. D., & Karniadakis, G. E. (2020). Physics-informed neural net-
673 works for high-speed flows. *Computer Methods in Applied Mechanics and Engi-
674 neering*, *360*, 112789.
- 675 Marras, S., Kelly, J. F., Moragues, M., Müller, A., Kopera, M. A., Vázquez, M., ...
676 Jorba, O. (2016). A review of element-based galerkin methods for numeri-
677 cal weather prediction: Finite elements, spectral elements, and discontinuous
678 galerkin. *Archives of Computational Methods in Engineering*, *23*(4), 673–722.
- 679 Molls, T., & Chaudhry, M. H. (1995). Depth-averaged open-channel flow model.
680 *Journal of Hydraulic Engineering*, *121*(6), 453–465.
- 681 Monnier, J., Couderc, F., Dartus, D., Larnier, K., Madec, R., & Vila, J.-P. (2016).
682 Inverse algorithms for 2d shallow water equations in presence of wet dry fronts:
683 Application to flood plain dynamics. *Advances in Water Resources*, *97*, 11–
684 24.
- 685 Morales-Hernández, M., Petaccia, G., Brufau, P., & García-Navarro, P. (2016).
686 Conservative 1d–2d coupled numerical strategies applied to river flooding: The
687 tiber (rome). *Applied Mathematical Modelling*, *40*(3), 2087–2105.
- 688 Pang, G., Lu, L., & Karniadakis, G. E. (2019). fpinns: Fractional physics-informed
689 neural networks. *SIAM Journal on Scientific Computing*, *41*(4), A2603–
690 A2626.
- 691 Paszke, A., Gross, S., Chintala, S., Chanan, G., Yang, E., DeVito, Z., ... Lerer, A.
692 (2017). Automatic differentiation in pytorch.
- 693 Raissi, M., Perdikaris, P., & Karniadakis, G. E. (2019). Physics-informed neural
694 networks: A deep learning framework for solving forward and inverse problems
695 involving nonlinear partial differential equations. *Journal of Computational
696 Physics*, *378*, 686–707.
- 697 Rastgoo, R., Kiani, K., Escalera, S., & Sabokrou, M. (2021). Sign language pro-
698 duction: A review. In *Proceedings of the ieee/cvf conference on computer vi-
699 sion and pattern recognition* (pp. 3451–3461).
- 700 Sanders, B. F., & Schubert, J. E. (2019). Primo: Parallel raster inundation model.
701 *Advances in Water Resources*, *126*, 79–95.
- 702 Shamkhalchian, A., & de Almeida, G. A. (2021). Upscaling the shallow water equa-
703 tions for fast flood modelling. *Journal of Hydraulic Research*, *59*(5), 739–756.
- 704 Smith, L. N., & Topin, N. (2019). Super-convergence: Very fast training of neu-
705 ral networks using large learning rates. In *Artificial intelligence and machine
706 learning for multi-domain operations applications* (Vol. 11006, p. 1100612).
- 707 Ștefănescu, R., Sandu, A., & Navon, I. M. (2014). Comparison of pod reduced or-
708 der strategies for the nonlinear 2d shallow water equations. *International Jour-
709 nal for Numerical Methods in Fluids*, *76*(8), 497–521.
- 710 Sulavko, A. (2020). Bayes-minkowski measure and building on its basis immune
711 machine learning algorithms for biometric facial identification. In *Journal of
712 physics: Conference series* (Vol. 1546, p. 012103).
- 713 Sun, L., Gao, H., Pan, S., & Wang, J.-X. (2020). Surrogate modeling for fluid flows
714 based on physics-constrained deep learning without simulation data. *Computer
715 Methods in Applied Mechanics and Engineering*, *361*, 112732.
- 716 Toro, E. F., & Garcia-Navarro, P. (2007). Godunov-type methods for free-surface
717 shallow flows: A review. *Journal of Hydraulic Research*, *45*(6), 736–751.
- 718 Vlassis, N. N., & Sun, W. (2021). Sobolev training of thermodynamic-informed neu-
719 ral networks for interpretable elasto-plasticity models with level set hardening.
720 *Computer Methods in Applied Mechanics and Engineering*, *377*, 113695.
- 721 Voulodimos, A., Doulamis, N., Doulamis, A., & Protopapadakis, E. (2018). Deep
722 learning for computer vision: A brief review. *Computational intelligence and
723 neuroscience*, *2018*.
- 724 William, W., Ware, A., Basaza-Ejiri, A. H., & Obungoloch, J. (2018). A review of

- 725 image analysis and machine learning techniques for automated cervical cancer
726 screening from pap-smear images. *Computer methods and programs in*
727 *biomedicine*, 164, 15–22.
- 728 Wilson, M., Bates, P., Alsdorf, D., Forsberg, B., Horritt, M., Melack, J., ... Famigli-
729 etti, J. (2007). Modeling large-scale inundation of amazonian seasonally
730 flooded wetlands. *Geophysical Research Letters*, 34(15).
- 731 Xin Qi, S. M., Gustavo A. M. de Almeida. (2023). *Dataset supporting an article*
732 *"physics informed neural networks for solving flow problems modeled by the*
733 *shallow water equations"* [dataset]. University of Southampton. Retrieved
734 from <https://doi.org/10.5258/SOTON/D2645> doi: 10.5258/SOTON/D2645
- 735 Yıldız, S., Goyal, P., Benner, P., & Karasözen, B. (2021). Learning reduced-order
736 dynamics for parametrized shallow water equations from data. *International*
737 *Journal for Numerical Methods in Fluids*, 93(8), 2803–2821.
- 738 Yoon, T. H., & Kang, S.-K. (2004). Finite volume model for two-dimensional shal-
739 low water flows on unstructured grids. *Journal of Hydraulic Engineering*,
740 130(7), 678–688.
- 741 Zhang, R., Liu, Y., & Sun, H. (2020). Physics-guided convolutional neural network
742 (phycnn) for data-driven seismic response modeling. *Engineering Structures*,
743 215, 110704.
- 744 Zhu, X. X., Tuia, D., Mou, L., Xia, G.-S., Zhang, L., Xu, F., & Fraundorfer, F.
745 (2017). Deep learning in remote sensing: A comprehensive review and list of
746 resources. *IEEE Geoscience and Remote Sensing Magazine*, 5(4), 8–36.
- 747 Zhu, Y., Zabararas, N., Koutsourelakis, P.-S., & Perdikaris, P. (2019). Physics-
748 constrained deep learning for high-dimensional surrogate modeling and uncer-
749 tainty quantification without labeled data. *Journal of Computational Physics*,
750 394, 56–81.

Appendix A PINN Design Experiments

This section illustrates the heuristic approach followed to determine the best possible design of the PINNs. We focus on Test 1, described in Section 3.1. All the PINNs shown in this section are trained from the same dataset resolved at 50 m resolution. Figures A1 and A2 show the accuracy (\mathcal{R}_h) of the PICNs and PIFCNs, respectively, as their architecture (number of layers and channels/neurons) is varied. In short, these figures show that it is difficult to conclude whether a single architecture can lead to significantly improved results, and we thus prioritize simplicity in our PINNs design. While this heuristic approach is, by definition, not guaranteed to find the optimal solution, it represents the summary of very many iterations. This holds for other tests and dataset resolutions considered in this study.

Similarly, we have tested three widely used activation functions: Relu, Sigmoid and Tanh (see Table A1). The chosen architecture for testing the PICN and PIFCN models is CNN-5-20 and FCNN-3(1000), respectively. For PICN, Sigmoid and Tanh display the same accuracy, while the result of the Relu-based PICN has higher errors. The PIFCN with Tanh yields better accuracy than using the other two activation functions. As a result, Tanh was chosen as the activation function to be employed in all PINNs discussed in this paper.

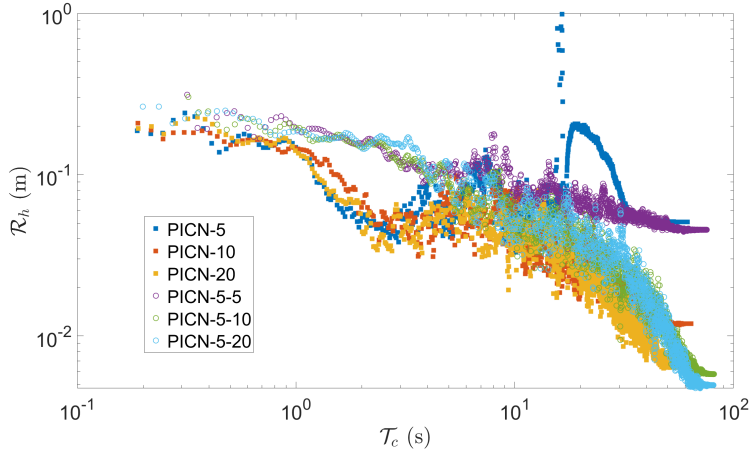


Figure A1. Comparison of PICNs with different architectures; the last hidden layer of all PICNs is one typical fully connected layer with 50 neurons. In the legend bar, the following format is adopted: PICN-X-Y, where the PICN has X channels in the first convolutional layer and Y channels in the second convolutional layer (thus, PICN-X denotes a network with one convolutional layer only).

Table A1. Results of water depth prediction by using Relu, Sigmoid and Tanh activation functions for PICN and PIFCN models. The trainset is a 50 m resolved dataset from Test 1; the evaluation metric is \mathcal{R}_h and its unit is m.

Model	Relu	Sigmoid	Tanh
PICN	0.021	0.002	0.002
PIFCN	0.154	0.028	0.004

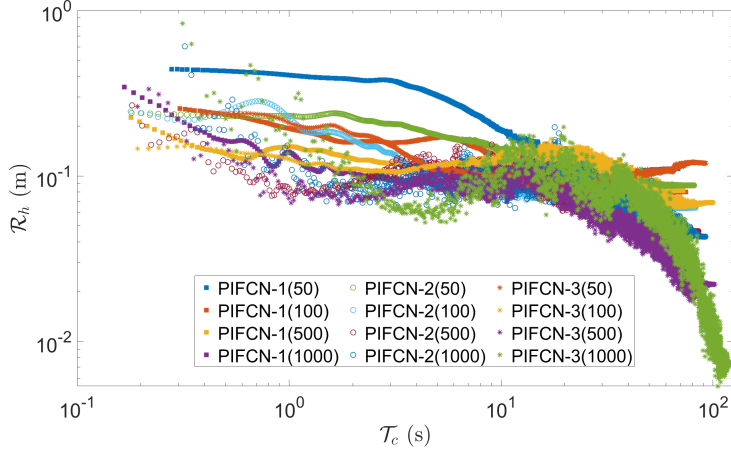


Figure A2. Comparison of PIFCNs with different architectures. In the legend bar, the following format is adopted: PIFCN-X(Y), where X denotes the number of hidden layers and Y is the number of neurons per layer.

769

Appendix B Further Spatial Analysis For Test 3

Table B1. Computation time and spatial prediction accuracy relative to benchmark simulation for the comparison. The unit for \mathcal{R}_h^s is m, and the unit for \mathcal{R}_{hu}^s and \mathcal{R}_{hv}^s is m^2s^{-1} .

Model name	\mathcal{T}_c (min)	t = 32 hours			t = 68 hours		
		\mathcal{R}_h^s	\mathcal{R}_{hu}^s	\mathcal{R}_{hv}^s	\mathcal{R}_h^s	\mathcal{R}_{hu}^s	\mathcal{R}_{hv}^s
PICN (50)	59.4	0.52	1.68	1.16	0.41	1.87	1.21
PICN (100)	15.3	0.40	1.72	1.18	0.37	1.92	1.20
PICN (200)	5.3	0.48	1.69	1.12	0.39	1.88	1.17
PIFCN (50)	504.9	0.59	2.21	1.32	0.52	2.21	1.28
PIFCN (100)	127.9	0.59	2.16	1.28	0.50	2.21	1.18
PIFCN (200)	30.2	0.63	2.27	1.21	0.47	2.16	1.15
FV (10)	2576.0	0.19	0.89	0.56	0.19	0.86	0.56
FV (25)	83.3	0.64	1.20	1.25	0.64	1.36	1.21
FV (50)	8.6	1.24	2.18	1.95	1.24	2.32	1.87

770

771

772

773

774

775

776

777

778

779

780

Table B1 summarizes the spatial prediction accuracy (i.e. \mathcal{R}_h^s , \mathcal{R}_{hu}^s , \mathcal{R}_{hv}^s) computed from a 50 m resolved set of points for each model at $t = 32$ and 68 hours, as well as their overall \mathcal{T}_c (i.e. training time for PINN and computation time for FV). Among all the models, FV (10) and FV (50) achieve the highest and lowest accuracy, respectively. All PINNs present lower \mathcal{R}_h^s than FV (25) and FV (50). On the other hand, FV (25) is more accurate than all PINNs in terms of hu prediction. PIFCN show a relatively similar value of \mathcal{R}_{hu}^s to FV (50) at both time points. Moreover, the prediction accuracy of the PICNs and PIFCNs is less affected by the resolution of the input dataset than in the FV model. This last point may potentially be a main advantage of PINNs relative to conventional numerical methods in general, whose performance (numerical stability and accuracy) tends to be highly dependent on the mesh resolution.